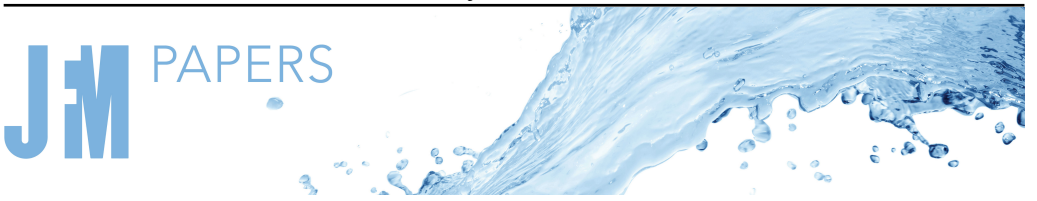
J. Fluid Mech. (2026), *vol.* 1042, A49, doi:10.1017/jfm.2026.11970



Analytical solutions for three-dimensional flow fields actuated by standing surface acoustic waves

Zekai Li[1], Yiming Li[1], Dongfang Liang[1], Yuning Zhang[2], Jian Zhou[3], Xin Yang[4] and Chen Fu[5]

[1]Department of Engineering, University of Cambridge, Cambridge CB2 1PZ, UK

[2]Key Laboratory of Power Station Energy Transfer Conversion and System (Ministry of Education), School of Energy Power and Mechanical Engineering, North China Electric Power University, Beijing 102206, PR China

[3]College of Mechanical and Vehicle Engineering, Hunan University, Changsha 410082, PR China

[4]School of Engineering, Cardiff University, Cardiff CF24 3AA, UK

[5]College of Physics and Optoelectronic Engineering, Shenzhen University, Shenzhen 518055, PR China

Corresponding authors: Dongfang Liang, dl359@cam.ac.uk; Yiming Li, yl842@cam.ac.uk

(Received 28 January 2026 UTC; revised 11 June 2026 UTC; accepted 23 July 2026 UTC)

This study develops a general theory for analysing a three-dimensional (3-D) acoustofluidic system, which consists of a cavity sandwiched by parallel piezoelectric substrates. The cavity is filled with a fluid and microparticle mixture, whose movements are actuated by surface acoustic waves (SAW) generated by the piezoelectric substrates. In contrast to the formulations based on the velocity potential and streamfunction, we developed a frequency-domain perturbation method to solve the compressible Navier–Stokes equations to obtain the acoustofluidic fields for both inviscid and viscous fluids. These solutions allow for the accurate prediction of the pressure nodal positions within the sandwiched cavity, and the effects of the microfluidic cavity geometry on the pressure nodal position are examined. Our analysis shows that the in-plane pressure-node distribution is controlled by phase modulation, whereas the out-of-plane distribution is governed by the amplitude ratio of the standing SAWs produced by the two parallel substrates. For viscous fluids, a coordinated amplitude–phase modulation strategy is proposed to achieve the desirable wave node distribution. The present theoretical derivations are validated against numerical simulations and laboratory experiments, in terms of both the velocity and pressure fields. This work provides guidelines for the

© The Author(s), 2026. Published by Cambridge University Press. This is an Open Access article, distributed under the terms of the Creative Commons Attribution licence (https://creativecommons.org/licenses/by/4.0/), which permits unrestricted re-use, distribution and reproduction, provided the original article is properly cited.

https://doi.org/10.1017/jfm.2026.11970 Published online by Cambridge University Press

fabrication and operation of acoustofluidic devices, extending current 2-D acoustic control to fully 3-D manipulation of microparticles suspended in the fluid.

Key words: microfluidics, acoustics

1. Introduction

Acoustofluidic systems have become an efficient, contact-free workbench for manipulating particles across a wide spectrum of applications (Luo *et al.* 2021; Stringer *et al.* 2023). When a surface acoustic wave (SAW) is coupled into a microchannel filled with a fluid and microparticle mixture, acoustic streaming and acoustic pressure fields are generated within the liquid, both of which exert significant influence on suspended particles depending on their physical properties (Nama *et al.* 2015). Specifically, smaller particles in the liquid are mainly affected by the Stokes drag force induced by acoustic streaming and thus move along the direction of the time-averaged stream velocity (Lighthill 1978), while larger particles are primarily influenced by the acoustic radiation force (King 1934; Doinikov 1994) and migrate toward the pressure nodes (PNs) or anti-pressure nodes (ANs) of the standing-wave field (Baudoin & Thomas 2020). Due to the versatility of SAWs, one can produce designated pressure distributions and streaming flow patterns for different functionalities. Leveraging theses mechanisms, SAW-based microfluidic devices have been widely applied in particle patterning (Bernard *et al.* 2017), mixing (Nam & Lim 2018), separation (Jo & Guldiken 2012) and manipulation (Ding *et al.* 2012).

Acoustic streaming between two opposing parallel plates has been studied extensively (Doinikov *et al.* 2017). The first analytical treatment was given by Lord Rayleigh in 1884, who described and explained the acoustic streaming of an incompressible fluid confined between two vibrating rigid walls (Rayleigh 1884). This shear-viscosity-dominated streaming driven by the viscous boundary layers has since become known as Rayleigh streaming. Carl Eckart (1948) later extended the scope of acoustic streaming, identifying an additional contribution from bulk viscosity that, together with shear viscosity, drives streaming throughout the fluid region. Streaming dominated by bulk viscosity is now termed Eckart streaming. A unified theoretical framework covering both Rayleigh and Eckart streaming, including time-dependent viscous effects, was subsequently established in Westervelt (1953). In recent years, the rapid growth of acoustofluidics has motivated renewed theoretical investigations into streaming produced by leaky SAWs (Muller *et al.* 2013; Doinikov *et al.* 2017).

For applications of acoustic streaming, it is widely applied for micromixing (Hsu & Liao 2025; Li *et al.* 2026) and for controlled rotation of microparticles (Friend & Yeo 2011; Shen *et al.* 2024). Surface-acoustic-wave-induced streaming generates an acoustic body force that drives bulk fluid motion within a confined chamber or a sessile droplet. This phenomenon occurs as the acoustic energy leaks from the piezoelectric substrate into the liquid, creating steady vortical structures. Particles entrained by these high-velocity streamlines are swept throughout the entire flow domain, and this convective mixing overcomes local concentration gradients and results in a homogeneous spatial distribution of the suspended particles (Stringer *et al.* 2023). While SAW-induced streaming is effective for bulk transport and mixing, it finds challenging in achieving stable localised particle trapping and patterning. Although streaming can keep particles circulating along defined orbital trajectories (Sun *et al.* 2025), it cannot achieve static equilibrium. Without further specialised boundary design or a radiation force, particles will always flow along these continuous streamlines due to the conservation of mass (Li *et al.* 2021).

https://doi.org/10.1017/jfm.2026.11970 Published online by Cambridge University Press

Consequently, tasks demanding accurate placement, e.g. patterning and translational manipulation, mostly rely on the acoustic pressure field instead (Melde *et al.* 2016).

Particle manipulation strategies that rely on the acoustic radiation force effectively overcome the limitations inherent in acoustic streaming. By tuning the phase of SAWs, the PNs of a standing surface acoustic wave (SSAW) can be positioned at specific locations. Therefore, the SSAW establishes highly localised potential energy wells in the adjacent fluid, and these spatial gradients exert a selective radiation force field that traps suspended microparticles along predictable trajectories (Baudoin & Thomas 2020). Sun *et al.* (2020) demonstrated a single-sided SAW configuration, where acoustic waves couple into the fluid from the bottom and establish a spatially tailored radiation force field. This configuration allowed for the migration of particles toward predesignated PNs, facilitating high-precision particle enrichment and concentration. Using the similar single-sided SAW set-up, Jo & Guldiken (2012) applied the acoustic field to drive particles laterally according to their density, achieving continuous, label-free sorting of a heterogeneous suspension. By integrating orthogonal sets of interdigital transducers (IDTs), the system extends from one-dimensional (1-D) lateral focusing to two-dimensional (2-D) planar control. A periodic matrix of PNs induced by 2-D SSAWs enables trapping and independent translation of microparticles across the entire substrate surface (Bernard *et al.* 2017), and by continuously modulating the phase of SSAWs, particles can move along user-defined trajectories (Ding *et al.* 2012). Yet, the degrees of freedom achievable with SSAWs generated from a single substrate plane are limited. Traditional devices with SSAWs originated from the bottom substrate enable precise in-plane particle manipulation within an XY plane, but out-of-plane control remains severely constrained by the fixed pressure nodal planes in the vertical direction. When out-of-plane particle displacement is required, particles can only be held at existing PNs by the acoustic radiation force, and further movement relies on balancing gravity and buoyancy, which is a compromise that offers poor spatio-temporal control (Shen *et al.* 2024). To address this limitation, we recently reported a novel acoustofluidic device design, which consists of two opposing substrates at the top and bottom of the fluid domain (Li *et al.* 2025*a*). This dual-sided configuration introduces an additional degree of freedom for acoustic radiation force-driven particle manipulation (Wang *et al.* 2023; Li *et al.* 2025*a*,*b*). Although the full particle manipulation capabilities of this architecture has not yet been experimentally characterised, a similar device have already demonstrated its effectiveness in high-efficiency micromixing (Nam & Lim 2018). Prior to 3-D particle control being realised with such dual-side-actuated SAW systems, a comprehensive mapping of the 3-D acoustic pressure distribution is essential.

In this study, we systematically analyse the dual-side-actuated SAW configuration using both analytical solutions and numerical simulations. Section 2 presents the governing equations and boundary conditions, together with the frequency-domain perturbation method, yielding closed-form analytical solutions for the first-order acoustic velocity and pressure fields for both Newtonian fluids and the inviscid fluids. The formulation is further extended to the time-averaged second-order acoustic streaming field. Section 3 validates the analytical solution against finite-element simulations and quantifies the influence of device geometry on the resulting pressure nodal structure. This section further demonstrates how out-of-plane pressure nodal planes can be positioned arbitrarily in both inviscid and viscous cases, providing valuable guidance for achieving accurate and flexible 3-D particle manipulation. The analytically predicted second-order streaming velocity distribution is also compared with numerical simulations to demonstrate the extension of the proposed perturbation analysis to the quasi-steady streaming flow. Finally, § 4 summarises the main findings and contributions of the study.

https://doi.org/10.1017/jfm.2026.11970 Published online by Cambridge University Press

2. Theory

This section presents the theoretical formulation of the SAW-driven acoustofluidic problem. We first introduce the general governing equations and the perturbation method for the first-order acoustic field in §§ 2.1 and 2.2. The boundary conditions and the frequency-domain approach adopted to derive the first-order solutions are then described in §§ 2.3–2.6. Finally, the formulation is extended in § 2.7 to describe the time-averaged second-order acoustic streaming field.

2.1. *Governing equations*

The continuity equation and Navier–Stokes equation for a viscous compressible fluid can be written as

$$\begin{cases} \dfrac{\partial \rho}{\partial t} + \boldsymbol{\nabla} \cdot (\rho \boldsymbol{v}) = 0, \\ \rho \dfrac{\partial \boldsymbol{v}}{\partial t} + \rho \left(\boldsymbol{v} \cdot \boldsymbol{\nabla}\right) \boldsymbol{v} = -\boldsymbol{\nabla} p + \mu \boldsymbol{\nabla}^2 \boldsymbol{v} + \left(\mu_b + \dfrac{\mu}{3}\right) \boldsymbol{\nabla} \left(\boldsymbol{\nabla} \cdot \boldsymbol{v}\right), \end{cases} \tag{2.1a}$$

where ρ, $\boldsymbol{v} = (u, v, w)$, p, μ and μ_b are the mass density, fluid velocity, fluid pressure, shear viscosity and bulk viscosity, respectively. For the acoustic field in the present SAW-driven cavity, the acoustic Mach number remains much smaller than unity, and the entropy variation induced by viscous dissipation and heat transfer is negligible (Li *et al.* 2023; Marques & Tomaz Da Silva 2025).Therefore, the thermodynamic relation between pressure and density is characterised by

$$c^2 = \left(\frac{\partial p}{\partial \rho}\right)_s, \tag{2.1b}$$

where c is the isentropic speed of sound in the liquid.

2.2. *Perturbation method*

The difficulty of solving the nonlinear terms in (2.1*a*) lies in the large time scale difference between the applied periodic ultrasonic oscillations with frequency, ranging from 1 to 100 MHz, and the induced nonlinear streaming flow with characteristic time spanning from tenths of a second to several minutes (Nama *et al.* 2015). Since the MHz acoustic excitation introduces only small perturbations to the fluid, the physical quantities are expanded in terms of a small non-dimensional parameter ϵ, which characterises the relative acoustic amplitude. For the present SAW-driven cavity, ϵ can be estimated by the acoustic Mach number based on the amplitude of the imposed velocity at the boundary, i.e.

$$\epsilon \sim Ma = W/c_0, \tag{2.2}$$

where Ma is the acoustic Mach number, W is the characteristic boundary velocity amplitude induced by the SAW excitation, as defined in (2.5), and c_0 is the speed of sound in water. For the present operating condition, $W \approx 0.01$ m s^{-1}, giving $Ma \approx 6 \times 10^{-6} \ll 1$. Therefore, following a small-amplitude perturbation approach (Köster 2007), the physical quantities are decomposed into the zeroth-order component (quiescent steady flow), the first-order component (harmonic oscillatory response), the second-order component (giving rise to the time-averaged acoustic streaming when averaged over an acoustic cycle) and higher-order small terms

$$\begin{cases} \boldsymbol{v} = \boldsymbol{v}_0 + \epsilon \boldsymbol{v}_1 + \epsilon^2 \boldsymbol{v}_2 + O(\epsilon^3), \\ p = p_0 + \epsilon p_1 + \epsilon^2 p_2 + O(\epsilon^3), \\ \rho = \rho_0 + \epsilon \rho_1 + \epsilon^2 \rho_2 + O(\epsilon^3), \end{cases} \tag{2.3}$$

https://doi.org/10.1017/jfm.2026.11970 Published online by Cambridge University Press

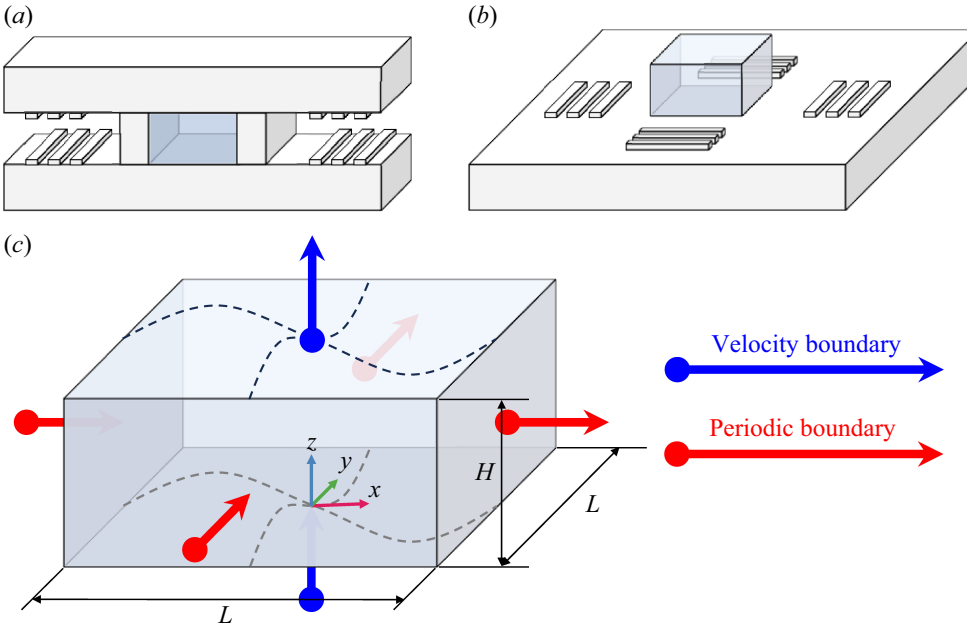


Figure 1. Schematic of the studied acoustofluidic models with different SAW configurations. (*a*) A microfluidic cavity whose bottom and top walls (or only the bottom wall) are piezoelectric substrates, each configured with a pair of opposing IDTs. The SAWs generated by these IDTs couple into the liquid and superpose. (*b*) A fluid chamber is configured on a substrate where two pairs of IDTs are orthogonally arranged to generate a 2-D SSAW field inside the fluid. (*c*) The fluid region is abstracted as a cubic domain. Red arrows indicate the direction in which periodic boundary conditions are applied, and blue arrows mark the positive direction of velocity boundary conditions.

where the subscripts 0, 1, 2 refer to the zeroth-order, first-order and the second-order components; $O(\epsilon^3)$ represent third-order small terms. Contributions beyond second order are assumed to be negligible and thus discarded.

Under the isentropic assumption in (2.1*b*), substituting (2.3) in to (2.1) and collecting only the first-order terms, we arrive at the linear governing equations

$$\begin{cases} \dfrac{\partial \rho_1}{\partial t} + \rho_0 \nabla \cdot \boldsymbol{v}_1 = 0, \\ \rho_0 \dfrac{\partial \boldsymbol{v}_1}{\partial t} = -\nabla p_1 + \mu \nabla^2 \boldsymbol{v}_1 + \left(\mu_b + \dfrac{\mu}{3}\right) \nabla \left(\nabla \cdot \boldsymbol{v}_1\right), \\ p_1 = c^2 \rho_1. \end{cases} \tag{2.4}$$

2.3. *Boundary conditions*

Typical SAW-based microfluidic systems consist of piezoelectric substrates, IDT pairs and microchannels. By applying an alternating current signal to the IDTs, SAWs are actuated on the surface of the piezoelectric substrate and propagate perpendicular to the orientation of the IDT fingers. The SAWs can be introduced into both continuous flows (figure 1*a*) and quiescent fluids (figure 1*b*), and the IDTs can be arranged in various configurations to generate controllable acoustofluidic field within the fluid domain. These devices can be abstracted to model as illustrated in figure 1(*c*), where the fluid domain is constrained in a cubic cavity with a height H and a square base of edge length L. The Eulerian reference

https://doi.org/10.1017/jfm.2026.11970 Published online by Cambridge University Press

frame $O(x, y, z)$ is placed at the centre of the bottom boundary of the liquid. Both the x and y axes are parallel to the plane of the substrates, and the axis z is perpendicular to the substrate plane. The upper and bottom boundaries are in direct contact with the piezoelectric substrates, through which leaky SAWs couple into the fluid. When a pair of IDTs is configured in parallel on opposite sides of the fluid cavity, counterpropagating SAWs form a 1-D SSAW. When two pairs of IDTs (four IDTs in total) are positioned orthogonally on a substrate (as shown in figure 1(*b*)), two orthogonal 1-D SSAWs interfere to form a 2-D SSAW field. Building on these traditional set-ups, we develop a model, for the first time, considering the SSAW fields in three dimensions, where 2-D SSAWs are formed simultaneously on both the upper and lower boundaries of the fluid region. With this framework, we systematically investigate the resulting 3-D acoustofluidic fields induced within the fluid domain by dual-sided 2-D SSAWs.

As the SAWs are spatially periodic along their propagation paths on the substrate (i.e. in the x- and y- directions), the resulting acoustofluidic field inherits this spatial periodicity when the substrate and fluid are assumed isotropic and the system operates in steady state. To utilise this property, we choose the edge lengths L of the square base of the domain to be an integer multiple of the SAW wavelength λ_{SAW}, thereby any physical quantity $Q(x, y, z, t)$, such as the velocity $\boldsymbol{v} = (u, v, w)$, pressure p and density ρ, takes the same value on opposing boundaries of the fluid domain in the x- and y- directions. Thus, periodic boundary conditions can be applied to four side boundaries of the fluid domain. Notably, setting the edge lengths of the base face of the cubic fluid domain to the same value L is not a requirement. This choice is made merely for convenience when expressing the periodic boundary conditions

$$\begin{cases} Q\left(-\dfrac{L}{2}, y, z, t\right) = Q\left(+\dfrac{L}{2}, y, z, t\right), \\ Q\left(x, -\dfrac{L}{2}, z, t\right) = Q\left(x, +\dfrac{L}{2}, z, t\right). \end{cases} \tag{2.5}$$

Because the top and bottom faces of the fluid domain (the surfaces normal to the z-direction) are in direct contact with the piezoelectric substrates, continuity requires that the substrates and the adjacent fluid share the same velocity. Therefore, as illustrated in figure 1(*c*), both the upper and lower surfaces of the fluid region are described by the velocity boundary conditions. Since the SAW excitation frequency is typically in the MHz range, which is several orders of magnitude higher than the characteristic time scales of particle migration and acoustic streaming, substrate vibration is treated as a steady, time-harmonic pattern that does not vary on the slow time scale of particle movement. For a single-frequency harmonic oscillation, the substrate surface displacement $\boldsymbol{u}_{sub}$ and velocity $\boldsymbol{v}$ are related by $\boldsymbol{v} = i\omega \boldsymbol{u}_{sub} Re(\exp(i\omega t))$. Therefore, imposing either a displacement or a velocity boundary condition is equivalent.

The velocity boundary condition that used to prescribe SAW propagation on the substrate has been reported in Li *et al.* (2023). The out-of-plane (along the z-direction) vibration generated by orthogonally aligned IDTs can be expressed as

$$\begin{cases} w_{+x,b}(x, y, 0, t) = W_{+x,b} \cdot Re(\exp(-C_{d,x}x - i(k_{SAW,x}x - \omega t + \varphi_{+x,b}))), \\ w_{-x,b}(x, y, 0, t) = W_{-x,b} \cdot Re(\exp(C_{d,x}x - i(-k_{SAW,x}x - \omega t + \varphi_{-x,b}))), \\ w_{+y,b}(x, y, 0, t) = W_{+y,b} \cdot Re(\exp(-C_{d,y}y - i(k_{SAW,y}y - \omega t + \varphi_{+y,b}))), \\ w_{-y,b}(x, y, 0, t) = W_{-y,b} \cdot Re(\exp(C_{d,y}y - i(-k_{SAW,y}y - \omega t + \varphi_{-y,b}))), \end{cases} \tag{2.6a}$$

https://doi.org/10.1017/jfm.2026.11970 Published online by Cambridge University Press

and

$$\begin{cases} w_{+x,t}\,(x,\,y,\,H,\,t) = W_{+x,t} \cdot Re(\exp(-C_{d,x}x - i(k_{SAW,x}x - \omega t + \varphi_{+x,t}))), \\ w_{-x,t}\,(x,\,y,\,H,\,t) = W_{-x,t} \cdot Re(\exp(C_{d,x}x - i(-k_{SAW,x}x - \omega t + \varphi_{-x,t}))), \\ w_{+y,t}\,(x,\,y,\,H,\,t) = W_{+y,t} \cdot Re(\exp(-C_{d,y}y - i(k_{SAW,y}y - \omega t + \varphi_{+y,t}))), \\ w_{-y,t}\,(x,\,y,\,H,\,t) = W_{-y,t} \cdot Re(\exp(C_{d,y}y - i(-k_{SAW,y}y - \omega t + \varphi_{-y,t}))), \end{cases} \tag{2.6b}$$

where $k_{SAW,x}$ and $k_{SAW,y}$ are the SAW wavenumbers along the x- and y-directions on the substrate, respectively; $C_{d,x}$ and $C_{d,y}$ are the corresponding attenuation coefficients of the SAWs along the x- and y-directions; φ and Wdenote the initial phase and velocity amplitude of each SAW component, respectively. The subscripts 'b' and 't' denote the bottom and top substrates, and the subscripts '+' and '–' identify waves travelling in the positive and negative directions of the corresponding axis, respectively. For instance, $\varphi_{+x,b}$ is the initial phase of the wave travelling in the $+x$ direction on the bottom substrate; i is the imaginary unit, i.e. $i = \sqrt{-1}$; $Re(\cdot)$ denotes the real-part operator; ω is the angular frequency of the substrate vibration. It should be noted that (2.6) prescribes only the out-of-plane substrate vibration velocity w. The in-plane vibration components u and v associated with the SAWs are neglected in the main text, since they are generally much smaller than the out-of-plane component in typical acoustofluidic systems (Jannesar & Hamzehpour 2021; Li *et al.* 2023).

For the analytical development in the main text, two further simplifications are adopted. First, for isotropic substrates, or for specially arranged actuation conditions under which the SAWs propagating along different in-plane directions exhibit the same propagation characteristics (Shen *et al.* 2024), one may take $k_{SAW,x} = k_{SAW,y} = k_{SAW}$ and $C_{d,x} = C_{d,y}$. Second, the attenuation coefficients $C_{d,x}$ and $C_{d,y}$ are neglected in the main text analysis. This approximation is commonly used in microfluidic applications, for which SAW attenuation over the characteristic propagation distance remains relatively weak. Specifically, with the attenuation coefficient reported by Nama *et al.* (2015), $C_d = 116\,\mathrm{m}^{-1}$, the wave amplitude still retains approximately 70 % of its initial value after propagating over 3000 µm. Accordingly, to keep the main derivation focused on the principal 3-D control mechanism, the attenuation terms are omitted in the main text.

Imposing velocity boundary conditions on both the top and bottom surfaces of the fluid domain is an approach of generalisation, rather than a specialisation. In practice, in addition to devices where the fluid channel is sandwiched between two piezoelectric substrates, there are also devices in which only one side of the channel is in contact with a vibrating substrate, while the opposite side interfaces a non-vibrating material. For such single-side-actuated devices, if the non-vibrating wall is acoustically rigid, we simply set the z-direction velocity amplitude in (2.6*b*) to zero, i.e. $W_{j,t} = 0$ or $W_{j,b} = 0$ ($j = +x, -x, +y, -y$), to enforce total reflection. If the non-vibrating wall is an acoustically soft material, the impedance boundary condition can be prescribed (Nama *et al.* 2015).

In (2.6), the reference phase is chosen as the mean of the initial phases of the two opposing travelling SAWs on the bottom substrate along the x-axis. To achieve independent control of the acoustic field in the x, y and z directions, SSAWs on the top and bottom substrates need to share the same vibration mode. Under this condition, the PNs and ANs of the 2-D SSAW fields on the top and bottom substrates are vertically aligned in the z-direction. Therefore, the eight initial phases of SAWs from the eight IDTs on the two substrates reduce to only four independent parameters

https://doi.org/10.1017/jfm.2026.11970 Published online by Cambridge University Press

$$\begin{cases} \varphi_{+x,b} = -\varphi_x, \\ \varphi_{-x,b} = \varphi_x, \\ \varphi_{+y,b} = -\varphi_y + \varphi_\Delta, \\ \varphi_{-y,b} = \varphi_y + \varphi_\Delta \end{cases} \tag{2.7a}$$

and

$$\begin{cases} \varphi_{+x,t} = -\varphi_x - \varphi_z, \\ \varphi_{-x,t} = \varphi_x - \varphi_z, \\ \varphi_{+y,t} = -\varphi_y + \varphi_\Delta - \varphi_z, \\ \varphi_{-y,t} = \varphi_y + \varphi_\Delta - \varphi_z \end{cases} \tag{2.7b}$$

Under this parameterisation, the phase difference between counter-propagating waves along the x-direction on both substrates is $2\varphi_x$; the phase difference between counter-propagating waves along the y-direction is $2\varphi_y$; the phase difference between SSAWs propagating along x- and y- directions is φ_Δ; and the phase difference between the SSAW fields on the two substrates is φ_z. While we operate reduction on initial phases, one still can get the analytical solutions of the linear governing equations in (2.4) using the method detailed in § 2.5 if every IDT is allowed its own independent phase (eight distinct values). Such fully arbitrary phase sets are, however, rare in practical device designs and lead to considerable mathematical complexity. Therefore, they are not further pursued in the main text.

To maintain a well-defined 2-D SSAW and avoid undesirable asymmetric wave fields, excitation of the four IDTs on each substrate with equal amplitude is assumed, i.e. $2W_{j,b} = W_b$ and $2W_{j,t} = W_t$ for $j = +x, -x, +y, -y$. The vibrations of the two substrates in (2.6) can be further condensed into (Bernard *et al.* 2017)

$$\begin{cases} w_b(x, y, 0, t) &= \sum_{j=+x,-x,+y,-y} w_{j,b}(x, y, 0, t) \\ &= W_b \cdot Re(\exp(i\omega t) \cdot (\cos(k_{SAW}x - \varphi_x) + \cos(k_{SAW}y - \varphi_y) \cdot \exp(-i\varphi_\Delta))), \\ w_t(x, y, H, t) &= \sum_{j=+x,-x,+y,-y} w_{j,t}(x, y, H, t) \\ &= W_t \cdot Re(\exp(i\omega t + i\varphi_z) \cdot (\cos(k_{SAW}x - \varphi_x) + \cos(k_{SAW}y - \varphi_y) \cdot \exp(-i\varphi_\Delta))), \end{cases} \tag{2.8a}$$

and

$$\begin{cases} u_b(x, y, 0, t) = u_t(x, y, H, t) = 0, \\ v_b(x, y, 0, t) = v_t(x, y, H, t) = 0, \end{cases} \tag{2.8b}$$

where $u_b(x, y, 0, t)$ and $u_t(x, y, H, t)$ are velocities along the x-direction; $v_b(x, y, 0, t)$ and $v_t(x, y, H, t)$ are velocities along the y-direction. Although an analytical solution for the acoustic field can still be derived when the IDTs operate at unequal amplitudes, this situation is rare in practice, and the resulting field is no longer a pure standing wave. Consequently, it is not discussed in the main text.

The above assumptions, however, are not intended to be universally valid. In particular, they may become inadequate when substrate anisotropy, elliptical motion or directional attenuation is significant. For this reason, a general form of boundary conditions and the corresponding analytical solutions without the above simplifications of material properties and parameterisation of initial phases are provided in the Supplementary Material where is available at https://doi.org/10.1017/jfm.2026.11970. Since the general formulation in the Supplementary Material leads to the same conclusions for the applications considered in § 3, the simplified form of the analytical solution under the approximations is adopted in this section.

https://doi.org/10.1017/jfm.2026.11970 Published online by Cambridge University Press

2.4. *Reduction of dimensions*

From (2.8), the total wave field on each substrate can be describe by the superposition of two SSAWs in the x- and y- directions, dependent on (x, z, t) or (y, z, t), respectively. Since (2.4) is linear, the 3-D problem can be reduced to the sum of two 2-D solutions. By this reduction of dimension, the original 2-D velocity boundary condition (2.8a) is decomposed to the sum of 1-D components as follows:

$$\begin{cases} w_b\,(x,\,y,\,0,\,t) = w_{x,b}\,(x,\,t) + w_{y,b}\,(y,\,t), \\ w_t\,(x,\,y,\,H,\,t) = w_{x,t}\,(x,\,t) + w_{y,t}\,(y,\,t), \end{cases} \tag{2.9}$$

where

$$\begin{cases} w_{x,b}(x,\,t) = W_b \cdot Re(\exp(i\omega t) \cdot \cos(k_{SAW}x - \varphi_x)), & (2.10a) \\ w_{y,b}(y,\,t) = W_b \cdot Re(\exp(i\omega t - i\varphi_\Delta) \cdot \cos(k_{SAW}y - \varphi_y)), & (2.10b) \\ w_{x,t}(x,\,t) = W_t \cdot Re(\exp(i\omega t + i\varphi_z) \cdot \cos(k_{SAW}x - \varphi_x)), & (2.10c) \\ w_{y,t}(y,\,t) = W_t \cdot Re(\exp(i\omega t - i\varphi_\Delta + i\varphi_z) \cdot \cos(k_{SAW}y - \varphi_y)). & (2.10d) \end{cases}$$

This decomposition yields two independent 2-D subproblems: one expressed with the independent variables (x, z, t) and the other with (y, z, t). Each can be solved separately, and the full 3-D solution to (2.4) is then obtained by superposing the two independent 2-D solutions. For example, considering the (x, z, t) subproblem, the boundary conditions (2.10a) and (2.10c) are applied, and the original 3-D governing equations reduce to the following 2-D form of (2.4):

$$\begin{cases} \dfrac{\partial \rho_1}{\partial t} + \rho_0 \left(\dfrac{\partial u_1}{\partial x} + \dfrac{\partial w_1}{\partial z} \right) = 0, \\ \rho_0 \dfrac{\partial u_1}{\partial t} = -\dfrac{\partial p_1}{\partial x} + \left(\dfrac{4\mu}{3} + \mu_b \right) \dfrac{\partial^2 u_1}{\partial x^2} + \mu \dfrac{\partial^2 u_1}{\partial z^2} + \left(\dfrac{\mu}{3} + \mu_b \right) \dfrac{\partial^2 w_1}{\partial x \partial z}, \\ \rho_0 \dfrac{\partial w_1}{\partial t} = -\dfrac{\partial p_1}{\partial z} + \left(\dfrac{4\mu}{3} + \mu_b \right) \dfrac{\partial^2 w_1}{\partial z^2} + \mu \dfrac{\partial^2 w_1}{\partial x^2} + \left(\dfrac{\mu}{3} + \mu_b \right) \dfrac{\partial^2 u_1}{\partial x \partial z}, \\ p_1 = c^2 \rho_1. \end{cases} \tag{2.11}$$

Figure 2 provides a geometric illustration of this dimensionality reduction. Taking the top substrate as an example, $w_{x,t}(x, t)$ corresponds to a SSAW that varies only along the x-direction and remains uniform along the y-direction; $w_{y,t}(y, t)$ corresponds to a SSAW that varies only along the y-direction. When these two components are superposed to form $w_t(x, y, H, t)$, a 2-D SSAW field is formed. The resulting 2-D SSAW patterns are dependent on the phase difference φ_Δ (Bernard *et al.* 2017). Yet, not every value of φ_Δ produces a qualitatively distinct pattern. Because $\exp(0) = 1$ and $\exp(i\pi/2) = i$, any phase-shifted wave with an arbitrary φ_Δ can be expressed as a linear combination of the two canonical cases shown in figure 2 ($\varphi_\Delta = 0$ and $\varphi_\Delta = \pi/2$). The different patterns illustrated in figure 2 are explained analytically later in § 3.2. The same property holds for the 2-D SSAW on the bottom substrate.

2.5. *First-order field for viscous fluid*

As discussed in § 2.3, the fluid domain is driven by boundary conditions that oscillate at a single frequency, thus the steady-state solution of (2.4) can be sought directly in the frequency domain. Furthermore, § 2.4 introduced the decomposition of the 3-D problem

https://doi.org/10.1017/jfm.2026.11970 Published online by Cambridge University Press

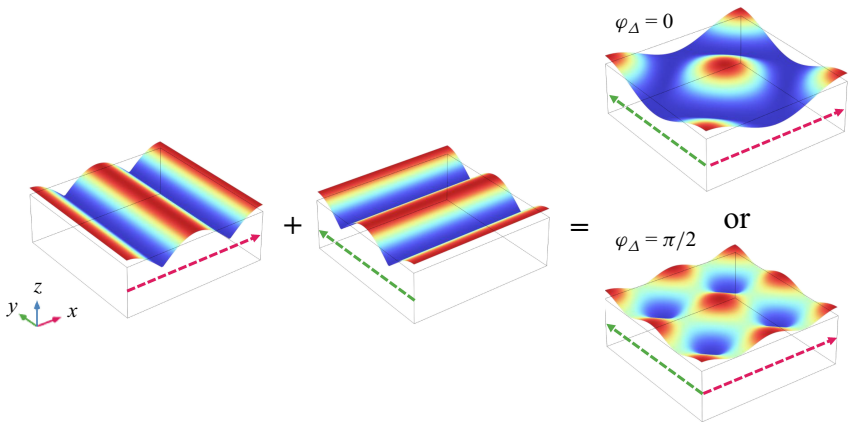


Figure 2. Geometric interpretation of reducing a 2-D SAW velocity boundary into a superposition of 1-D SAWs.

to the sum of 2-D subproblems. Without loss of generality, we first examine the (x, z, t)-dependent 2-D subproblem

$$\begin{cases} \boldsymbol{v}_1 = Re\left(\dfrac{\widetilde{\boldsymbol{V}}(z)}{2} \cdot \left(\exp\left(i\omega t - ik_{SAW}x + i\varphi_x\right) + \exp\left(i\omega t + ik_{SAW}x - i\varphi_x\right)\right)\right), \\ p_1 = Re\left(\dfrac{\tilde{P}(z)}{2} \cdot \left(\exp\left(i\omega t - ik_{SAW}x + i\varphi_x\right) + \exp\left(i\omega t + ik_{SAW}x - i\varphi_x\right)\right)\right), \\ \rho_1 = Re\left(\dfrac{\tilde{\rho}(z)}{2} \cdot \left(\exp\left(i\omega t - ik_{SAW}x + i\varphi_x\right) + \exp\left(i\omega t + ik_{SAW}x - i\varphi_x\right)\right)\right). \end{cases} \tag{2.12}$$

Here, the tilde '$\tilde{\cdot}$' denotes the complex amplitude independent of time, and $\widetilde{\boldsymbol{V}}(z) = (\tilde{U}(z), \tilde{V}(z), \tilde{W}(z))$. For every variable defined in (2.12), we can solve separately for the components containing $\exp(i\omega t - ik_{SAW}x + i\varphi_x)$ and $\exp(i\omega t + ik_{SAW}x - i\varphi_x)$. Any first-order quantity Q_1, e.g. $\boldsymbol{v}_1$, p_1, ρ_1, can therefore be decomposed as

$$\begin{cases} Q_1 = Re\left(Q_{1,+} + Q_{1,-}\right), & (2.13a) \\ Q_{1,+} = \dfrac{\tilde{Q}(z)}{2} \cdot \exp\left(i\omega t + ik_{SAW}x - i\varphi_x\right), & (2.13b) \\ Q_{1,-} = \dfrac{\tilde{Q}(z)}{2} \cdot \exp\left(i\omega t - ik_{SAW}x + i\varphi_x\right), & (2.13c) \end{cases}$$

where $Q_{1,+}$ represents any first-order quantity carrying component of $\exp(i\omega t + ik_{SAW}x - i\varphi_x)$, and the first-order quantities $Q_{1,+}$ and $Q_{1,-}$ are formally symmetric. We therefore first solve for the component $Q_{1,+}$. The decomposition in (2.13) shows that $Q_{1,+}$ satisfies

$$\begin{cases} \dfrac{\partial Q_{1,+}}{\partial x} = ik_{SAW}Q_{1,+}, \\ \dfrac{\partial Q_{1,+}}{\partial t} = i\omega Q_{1,+}. \end{cases} \tag{2.14}$$

https://doi.org/10.1017/jfm.2026.11970 Published online by Cambridge University Press

Substituting the decomposed $Q_{1,+}$ into (2.11), we obtain the following ordinary differential equations (ODEs) in the variable z:

$$\begin{cases} i\omega\rho_{1,+} + \rho_0\left(ik_{SAW}u_{1,+} + \dfrac{\mathrm{d}w_{1,+}}{\mathrm{d}z}\right) = 0, & (2.15a) \\ i\omega\rho_0 u_{1,+} = -ik_{SAW}p_{1,+} - \left(\dfrac{4\mu}{3} + \mu_b\right)k_{SAW}^2 u_{1,+} + \mu\dfrac{\mathrm{d}^2u_{1,+}}{\mathrm{d}z^2} + ik_{SAW}\left(\dfrac{\mu}{3} + \mu_b\right)\dfrac{\mathrm{d}w_{1,+}}{\mathrm{d}z}, & (2.15b) \\ i\omega\rho_0 w_{1,+} = -\dfrac{\mathrm{d}p_{1,+}}{\mathrm{d}z} + \left(\dfrac{4\mu}{3} + \mu_b\right)\dfrac{\mathrm{d}^2w_{1,+}}{\mathrm{d}z^2} - \mu k_{SAW}^2 w_{1,+} + ik_{SAW}\left(\dfrac{\mu}{3} + \mu_b\right)\dfrac{\mathrm{d}u_{1,+}}{\mathrm{d}z}, & (2.15c) \\ p_{1,+} = c^2\rho_{1,+}. & (2.15d) \end{cases}$$

Eliminating $\rho_{1,+}$ by substituting (2.15d) into (2.15a) yields

$$i\omega p_{1,+} + \rho_0 c^2\left(ik_{SAW}u_{1,+} + \frac{\mathrm{d}w_{1,+}}{\mathrm{d}z}\right) = 0. \tag{2.16}$$

Substituting (2.16) into (2.15b) and (2.15c) gives

$$\begin{cases} i\omega\rho_0 u_{1,+} = k_{SAW}\dfrac{\rho_0 c^2}{\omega}\left(ik_{SAW}u_{1,+} + \dfrac{\mathrm{d}w_{1,+}}{\mathrm{d}z}\right) - \left(\dfrac{4\mu}{3} + \mu_b\right)k_{SAW}^2 u_{1,+} + \mu\dfrac{\mathrm{d}^2u_{1,+}}{\mathrm{d}z^2} + ik_{SAW}\left(\dfrac{\mu}{3} + \mu_b\right)\dfrac{\mathrm{d}w_{1,+}}{\mathrm{d}z}, \\ i\omega\rho_0 w_{1,+} = -i\dfrac{\rho_0 c^2}{\omega}\left(ik_{SAW}\dfrac{\mathrm{d}u_{1,+}}{\mathrm{d}z} + \dfrac{\mathrm{d}^2w_{1,+}}{\mathrm{d}z^2}\right) + \left(\dfrac{4\mu}{3} + \mu_b\right)\dfrac{\mathrm{d}^2w_{1,+}}{\mathrm{d}z^2} - \mu k_{SAW}^2 w_{1,+} + ik_{SAW}\left(\dfrac{\mu}{3} + \mu_b\right)\dfrac{\mathrm{d}u_{1,+}}{\mathrm{d}z}. \end{cases} \tag{2.17}$$

Equation (2.17) includes a set of coupled, second-order, linear, homogeneous ODEs. For a viscous fluid they can be solved by an eigen-mode (characteristic-mode) method. Setting $\boldsymbol{\Gamma}_+ = [\ u_{1,+} \quad w_{1,+}\ ]^T$, then (2.17) can be rewritten as

$$\boldsymbol{M_2}\frac{\mathrm{d}^2\boldsymbol{\Gamma}_+}{\mathrm{d}z^2} + \boldsymbol{M_1}\frac{\mathrm{d}\boldsymbol{\Gamma}_+}{\mathrm{d}z} + \boldsymbol{M_0}\boldsymbol{\Gamma}_+ = 0, \tag{2.18}$$

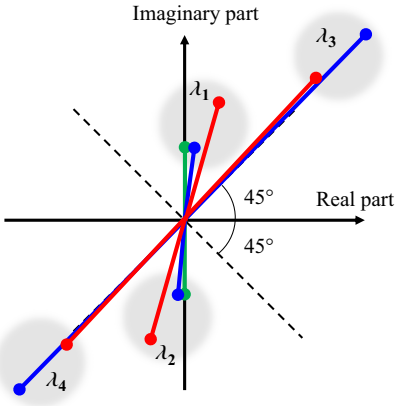
where

$$\begin{cases} \boldsymbol{M_2} = \begin{bmatrix} \mu & 0 \\ 0 & \left(\dfrac{4\mu}{3} + \mu_b\right) - i\dfrac{\rho_0 c^2}{\omega} \end{bmatrix}, \\ \boldsymbol{M_1} = \begin{bmatrix} 0 & k_{SAW}\dfrac{\rho_0 c^2}{\omega} + ik_{SAW}\left(\dfrac{\mu}{3} + \mu_b\right) \\ k_{SAW}\dfrac{\rho_0 c^2}{\omega} + ik_{SAW}\left(\dfrac{\mu}{3} + \mu_b\right) & 0 \end{bmatrix}, \\ \boldsymbol{M_0} = \begin{bmatrix} -i\omega\rho_0 + ik_{SAW}^2\dfrac{\rho_0 c^2}{\omega} - \left(\dfrac{4\mu}{3} + \mu_b\right)k_{SAW}^2 & 0 \\ 0 & -i\omega\rho_0 - \mu k_{SAW}^2 \end{bmatrix}. \end{cases} \tag{2.19}$$

Owing to the linearity of (2.17), its solution can be sought in the form

$$\boldsymbol{\Gamma}_+ = \sum_{j=1,2,3,4} C_{+,j}\boldsymbol{E}_{+,j}\exp\left(\lambda_{+,j}z\right)\cdot\exp\left(i\omega t + ik_{SAW}x - i\varphi_x\right), \tag{2.20}$$

https://doi.org/10.1017/jfm.2026.11970 Published online by Cambridge University Press



	Engine oil	Water	Inviscid water
μ (Pa · s)	0.790	1.01×10^{-3}	0
μ_B (Pa · s)	0.790	2.82×10^{-3}	0
$\lambda_1 = -\lambda_2$ ($\times 10^3$ m^{-1})	$7.36 + 80i$	$0.004 + 52.4i$	$52.4i$
$\lambda_4 = -\lambda_3$ ($\times 10^3$ m^{-1})	$216.1 + 217.1i$	$6428 + 6428i$	—

Figure 3. Eigenvalue spectra for liquids of different viscosities.

where the coefficients $C_{+,j}$ are constants determined by the boundary conditions; $\boldsymbol{E}_{+,j}$ is the generalised eigenvector (independent of x, z and t) and $\lambda_{+,j}$ is the corresponding generalised eigenvalue.

Substituting (2.20) into (2.18) yields

$$\begin{bmatrix} \lambda_{+,j}^2\mu - \left(i\omega\rho_0 + k_{SAW}^2 R\right) & \lambda_{+,j} i k_{SAW}(R-\mu) \\ \lambda_{+,j} i k_{SAW}(R-\mu) & \lambda_{+,j}^2 R - i\omega\rho_0 - \mu k_{SAW}^2 \end{bmatrix} \boldsymbol{E}_{+,j} = 0, \tag{2.21}$$

where $R = (((4\mu)/3) + \mu_b) - i((\rho_0 c^2)/\omega)$.

Taking the determinant of the matrix in (2.21) and setting it to zero gives a quartic algebraic equation for $\lambda_{+,j}$

$$\begin{aligned} \mu R\lambda_{+,j}^4 - \left(Ri\omega\rho_0 + \mu\left(i\omega\rho_0 + 2Rk_{SAW}^2\right)\right)\lambda_{+,j}^2 \\ + \left(i\omega\rho_0 + k_{SAW}^2 R\right)\left(i\omega\rho_0 + \mu k_{SAW}^2\right) = 0. \end{aligned} \tag{2.22}$$

Solving this quartic equation yields four roots for $\lambda_{+,j}$, which correspond to the four generalised eigenvalues of (2.21). Since (2.22) contains only even powers of $\lambda_{+,j}$, the eigenvalues can be written as

$$\begin{aligned} \lambda_{+,j} = \pm (2\mu R)^{-\frac{1}{2}} \Big(i\omega\rho_0 R + \mu\left(i\omega\rho_0 + 2Rk_{SAW}^2\right) \pm \Big(\left(i\omega\rho_0 R + \mu\left(i\omega\rho_0 + 2Rk_{SAW}^2\right)\right)^2 \\ -4\mu R\left(i\omega\rho_0 + k_{SAW}^2 R\right)\left(i\omega\rho_0 + \mu k_{SAW}^2\right)\Big)^{\frac{1}{2}} \Big)^{\frac{1}{2}}. \end{aligned} \tag{2.23}$$

Figure 3 shows the generalised eigenvalues $\lambda_{+,j}$ computed from (2.23) for different liquids. For an ideally inviscid liquid, only two finite eigenvalues exist and both are purely imaginary. For low-viscosity liquids such as water, two additional eigenvalues with large magnitudes appear at approximately 45° and −135° in the complex plane, while the remaining eigenvalues cluster near the imaginary axis. For high-viscosity liquids such as engine oil, four eigenvalues of comparable magnitude emerge, symmetrically distributed across the first and third quadrants. Both the highly viscous engine oil and the less viscous water have four eigenvalues, where $\lambda_{+,3}$ and $\lambda_{+,4}$ exhibit a markedly larger real part than $\lambda_{+,1}$ and $\lambda_{+,2}$. These real components $\lambda_{+,3}$ and $\lambda_{+,4}$ account for viscous dissipation near the boundary layer, which will be explained later. In contrast, $\lambda_{+,1}$ and $\lambda_{+,2}$ are almost

https://doi.org/10.1017/jfm.2026.11970 Published online by Cambridge University Press

purely imaginary, representing a bulk acoustic wave (BAW) outside the boundary layer. In § 3.4 we will compare how the boundary-layer thickness varies with the real parts of $\lambda_{+,3}$ and $\lambda_{+,4}$ for fluids of different viscosities.

From (2.23) we obtain the four distinct generalised eigenvalues $\lambda_{+,j}(\mu, \mu_b, \omega, \rho_0, c, k_{SAW})$, $j = 1, 2, 3, 4$, of the $\boldsymbol{\Gamma}_+$ field. To obtain the generalised eigenvalues $\lambda_{-,j}$ for the companion field $\boldsymbol{\Gamma}_-$, one can reverse the sign of every k_{SAW} appearing in the matrix of (2.21) and re-evaluate the eigenvalues of matrix in the following equation:

$$\begin{bmatrix} \lambda_{-,j}^2\mu - \left(i\omega\rho_0 + k_{SAW}^2 R\right) & -\lambda_{-,j} i k_{SAW}(R-\mu) \\ -\lambda_{-,j} i k_{SAW}(R-\mu) & \lambda_{-,j}^2 R - i\omega\rho_0 - \mu k_{SAW}^2 \end{bmatrix} \boldsymbol{E}_{-,j} = 0. \tag{2.24}$$

From the structure of (2.24) and (2.21), one can find that $\lambda_{+,j} = \lambda_{-,j}$. Henceforth, we simply use λ_j for either set.

Inserting the generalised eigenvalues λ_j into (2.21) and (2.24) gives the generalised eigenvectors $\boldsymbol{E}_{+,j}$ and $\boldsymbol{E}_{-,j}$. Writing them in terms of velocity components as $\boldsymbol{E}_{+,j} = [E^u_{+,j} \;\; E^w_{+,j}]^T$ and $\boldsymbol{E}_{-,j} = [E^u_{-,j} \;\; E^w_{-,j}]^T$ obtains

$$\begin{cases} E^u_{+,j} = i\dfrac{\lambda_j^2 R - i\omega\rho_0 - \mu k_{SAW}^2}{\lambda_j k_{SAW}(R-\mu)}, \\ E^w_{+,j} = 1, \end{cases} \tag{2.25a}$$

and

$$\begin{cases} E^u_{-,j} = -E^u_{+,j}, \\ E^w_{-,j} = E^w_{+,j}. \end{cases} \tag{2.25b}$$

Because (2.4) is linear, the velocity amplitudes W_b and W_t prescribed by the boundary conditions (2.10) can be separated from the constants $C_{+,j}$ in (2.20)

$$C_{+,j} = C_{+,b,j}\frac{W_b}{2} + C_{+,t,j}\frac{W_t \exp(i\varphi_z)}{2}. \tag{2.26a}$$

Symmetrically,

$$C_{-,j} = C_{-,b,j}\frac{W_b}{2} + C_{-,t,j}\frac{W_t \exp(i\varphi_z)}{2}. \tag{2.26b}$$

According to the definitions of $C_{+,b,j}$ and $C_{+,t,j}$ in (2.26), the constants can be found in

$$\begin{bmatrix} E^u_{+,1} & E^u_{+,2} & E^u_{+,3} & E^u_{+,4} \\ E^w_{+,1} & E^w_{+,2} & E^w_{+,3} & E^w_{+,4} \\ E^u_{+,1}\exp(\lambda_1 H) & E^u_{+,2}\exp(\lambda_2 H) & E^u_{+,3}\exp(\lambda_3 H) & E^u_{+,4}\exp(\lambda_4 H) \\ E^w_{+,1}\exp(\lambda_1 H) & E^w_{+,2}\exp(\lambda_2 H) & E^w_{+,3}\exp(\lambda_3 H) & E^w_{+,4}\exp(\lambda_4 H) \end{bmatrix} \begin{bmatrix} C_{+,b,1} \\ C_{+,b,2} \\ C_{+,b,3} \\ C_{+,b,4} \end{bmatrix} = \begin{bmatrix} 0 \\ 1 \\ 0 \\ 0 \end{bmatrix}, \tag{2.27a}$$

and

$$\begin{bmatrix} E^u_{+,1} & E^u_{+,2} & E^u_{+,3} & E^u_{+,4} \\ E^w_{+,1} & E^w_{+,2} & E^w_{+,3} & E^w_{+,4} \\ E^u_{+,1}\exp(\lambda_1 H) & E^u_{+,2}\exp(\lambda_2 H) & E^u_{+,3}\exp(\lambda_3 H) & E^u_{+,4}\exp(\lambda_4 H) \\ E^w_{+,1}\exp(\lambda_1 H) & E^w_{+,2}\exp(\lambda_2 H) & E^w_{+,3}\exp(\lambda_3 H) & E^w_{+,4}\exp(\lambda_4 H) \end{bmatrix} \begin{bmatrix} C_{+,t,1} \\ C_{+,t,2} \\ C_{+,t,3} \\ C_{+,t,4} \end{bmatrix} = \begin{bmatrix} 0 \\ 0 \\ 0 \\ 1 \end{bmatrix}. \tag{2.27b}$$

https://doi.org/10.1017/jfm.2026.11970 Published online by Cambridge University Press

Replacing every subscript '+' with '–' in (2.27) gives the analogous expressions for $C_{-,b,j}$ and $C_{-,t,j}$ that satisfy the boundary conditions. Inserting the relation between $\boldsymbol{E}_{+,j}$ and $\boldsymbol{E}_{-,j}$ from (2.25) into (2.27) yields

$$\begin{cases} C_{+,b,j} = C_{-,b,j}, \\ C_{+,t,j} = C_{-,t,j}. \end{cases} \tag{2.28}$$

Consequently, we no longer distinguish between $C_{+,b,j}$ and $C_{-,b,j}$, and denote both as $C_{b,j}$. Likewise, $C_{+,t,j}$ and $C_{-,t,j}$ are both written as $C_{t,j}$.

Inserting the expressions for $C_{b,j}$ and $C_{t,j}$ obtained from (2.27), together with the generalised eigenvalues in (2.23) and eigenvectors in (2.25), into (2.20) gives

$$\boldsymbol{\Gamma}_{+} = \sum_{j=1,2,3,4} \left(C_{b,j} \frac{W_b}{2} + C_{t,j} \frac{W_t \exp(i\varphi_z)}{2} \right) \boldsymbol{E}_{+,j} \exp(\lambda_j z) \cdot \exp(i\omega t + ik_{SAW}x - i\varphi_x). \tag{2.29a}$$

Symmetrically,

$$\boldsymbol{\Gamma}_{-} = \sum_{j=1,2,3,4} \left(C_{b,j} \frac{W_b}{2} + C_{t,j} \frac{W_t \exp(i\varphi_z)}{2} \right) \boldsymbol{E}_{-,j} \exp(\lambda_j z) \cdot \exp(i\omega t - ik_{SAW}x + i\varphi_x). \tag{2.29b}$$

Combining (2.29*a*) and (2.29*b*) for the (x, z, t) subproblem and simplifying the equations yields

$$\begin{aligned} \begin{bmatrix} u_1 \\ w_1 \end{bmatrix} &= \boldsymbol{\Gamma} = Re\left(\boldsymbol{\Gamma}_{+} + \boldsymbol{\Gamma}_{-}\right) \\ &= Re\left(\exp(i\omega t) \cdot \sum_{j=1,2,3,4} \begin{bmatrix} -\dfrac{\lambda_j^2 R - i\omega\rho_0 - \mu k_{SAW}^2}{\lambda_j k_{SAW}(R-\mu)} \sin(k_{SAW}x - \varphi_x) \\ \cos(k_{SAW}x - \varphi_x) \end{bmatrix} \left(C_{b,j} W_b + C_{t,j} W_t \exp(i\varphi_z) \right) \exp(\lambda_j z) \right). \end{aligned} \tag{2.30}$$

Applying the same procedure outlined in (2.12)–(2.30) to the (y, t)-dependent boundary conditions given by (2.10*b*) and (2.10*d*), we obtain the corresponding (y, z, t) subproblem. Superposing these 2-D solutions gives the complete 3-D first-order velocity field

$$\begin{cases} u_1 = Re\left(-\exp(i\omega t) \sin(k_{SAW}x - \varphi_x) \sum_{j=1,2,3,4} \dfrac{\lambda_j^2 R - i\omega\rho_0 - \mu k_{SAW}^2}{\lambda_j k_{SAW}(R-\mu)} \left(C_{b,j} W_b + C_{t,j} W_t \exp(i\varphi_z) \right) \exp(\lambda_j z) \right), \\ v_1 = Re\left(-\exp(i\omega t - i\varphi_\Delta) \sin(k_{SAW}y - \varphi_y) \sum_{j=1,2,3,4} \dfrac{\lambda_j^2 R - i\omega\rho_0 - \mu k_{SAW}^2}{\lambda_j k_{SAW}(R-\mu)} \left(C_{b,j} W_b + C_{t,j} W_t \exp(i\varphi_z) \right) \exp(\lambda_j z) \right), \\ w_1 = Re\Big(\exp(i\omega t) \sum_{j=1,2,3,4} \left(C_{b,j} W_b + C_{t,j} W_t \exp(i\varphi_z) \right) \exp(\lambda_j z) \\ \qquad \cdot \left(\cos(k_{SAW}x - \varphi_x) + \exp(-i\varphi_\Delta) \cos(k_{SAW}y - \varphi_y) \right) \Big), \end{cases} \tag{2.31}$$

https://doi.org/10.1017/jfm.2026.11970 Published online by Cambridge University Press

and the first-order pressure and density fields

$$\begin{cases} p_1 = c^2\rho_1, \\ \rho_1 = Re(i\frac{\rho_0}{\omega}\exp(i\omega t)\sum_{j=1,2,3,4}\left(\frac{i\omega\rho_0+\mu k_{SAW}^2-\lambda_j^2\mu}{\lambda_j(R-\mu)}\right)(C_{b,j}W_b + C_{t,j}W_t\exp(i\varphi_z))\exp(\lambda_j z) \\ \quad \cdot(\cos(k_{SAW}x-\varphi_x)+\exp(-i\varphi_\Delta)\cos(k_{SAW}y-\varphi_y))), \end{cases} \tag{2.32}$$

where $C_{b,j}$ and $C_{t,j}$, defined in (2.27), are functions of $\mu, \mu_b, \omega, \rho_0, c, k_{SAW}, H$. Equations (2.31) and (2.32) give the complete first-order solution for the viscous case. These first-order velocity, pressure and density fields also provide the basis for constructing the time-averaged second-order acoustic streaming field, which will be formulated in § 2.7. Before introducing the second-order extension, we first complete the discussion of the first-order problem by considering the inviscid limit in § 2.6.

2.6. *First-order field for inviscid fluid*

As seen in figure 3, for the case of water, the eigenvalues λ_3 and λ_4 (which represent viscous dissipation) are much larger in magnitude than λ_1 and λ_2 (which describe BAW propagation). This implies that the characteristic dissipation length in water is far shorter than the BAW wavelength. Consequently, for microfluidic applications that use water or other low-viscosity fluids, viscous dissipation can be neglected in almost the entire interested region, yielding a compact closed-form solution. Dropping viscosity by removing the highest-order coefficient in (2.21) yields

$$-c^2\lambda_{+,j}^2 - \omega^2 + k_{SAW}^2c^2 = 0, \tag{2.33}$$

where we can solve the two roots for λ_+, as follows:

$$\begin{cases} \lambda_{+,1} = ik_\perp, \\ \lambda_{+,2} = -ik_\perp, \end{cases} \tag{2.34}$$

and

$$k_\perp = \sqrt{k_f^2 - k_{SAW}^2}, \tag{2.35}$$

where $k_f = (\omega/c)$ is the wavenumber in water, and the physical meaning of $k_\perp$ will be discussed further in § 3.3.

Similarly, (2.21) is simplified under the inviscid assumption

$$\begin{bmatrix} -i\omega + ik_{SAW}^2\frac{c^2}{\omega} & \lambda_+\left(k_{SAW}\frac{c^2}{\omega}\right) \\ \lambda_+\left(k_{SAW}\frac{c^2}{\omega}\right) & -i\frac{c^2}{\omega}\lambda_+^2 - i\omega \end{bmatrix} \boldsymbol{E}_{+,j} = 0. \tag{2.36}$$

Inserting the eigenvalues obtained from (2.34) into (2.36) yields the eigenvectors

$$\begin{cases} E_{+,1} = \begin{bmatrix} k_{SAW}/k_\perp & 1 \end{bmatrix}^T, \\ E_{+,2} = \begin{bmatrix} -k_{SAW}/k_\perp & 1 \end{bmatrix}^T. \end{cases} \tag{2.37}$$

Substituting the eigenvectors in (2.37) and the eigenvalues in (2.34) into (2.20), and imposing the boundary conditions (2.10*a*) and (2.10*c*) in the form of (2.11), C_1 and C_2 can

https://doi.org/10.1017/jfm.2026.11970 Published online by Cambridge University Press

be solved by

$$\begin{cases} w_{1,+}(x,\, z=0,\, t) = \dfrac{W_b}{2} \cdot \exp(i\omega t + ik_{SAW}x - i\varphi_x) = (C_1 + C_2)\exp(i\omega t + ik_{SAW}x - i\varphi_x), \\ w_{1,+}(x,\, z=H,\, t) = \dfrac{W_t \exp(i\varphi_z)}{2} \cdot \exp(i\omega t + ik_{SAW}x - i\varphi_x) \\ \qquad\qquad = \big(C_1 \exp(H\lambda_{+,1}) + C_2 \exp(H\lambda_{+,2})\big)\exp(i\omega t + ik_{SAW}x - i\varphi_x), \end{cases} \tag{2.38}$$

i.e.

$$\begin{cases} \dfrac{W_b}{2} = C_1 + C_2, \\ \dfrac{W_t \exp(i\varphi_z)}{2} = (C_1 \exp(iHk_\perp) + C_2 \exp(-iHk_\perp)). \end{cases} \tag{2.39}$$

Solving (2.39) for C_1 and C_2 gives

$$\begin{cases} C_1 = \dfrac{W_t \exp(i\varphi_z) - W_b \exp(-iHk_\perp)}{4i \sin(Hk_\perp)}, \\ C_2 = \dfrac{W_b}{2} - \dfrac{W_t \exp(i\varphi_z) - W_b \exp(-iHk_\perp)}{4i \sin(Hk_\perp)}. \end{cases} \tag{2.40}$$

Following the same procedure outlined in (2.14)–(2.22) and (2.33)–(2.40), we obtain the complementary components $\boldsymbol{v}_{1,-}$, $p_{1,-}$ and $\rho_{1,-}$ defined by the decomposition (2.12). Inserting (2.40) into (2.20) and then summing $\boldsymbol{v}_{1,+}$ and $\boldsymbol{v}_{1,-}$ according to (2.13*a*) yields the first-order velocity field that satisfies the boundary conditions (2.9*a*) and (2.9*c*)

$$\begin{cases} u_1 = Re\left(\exp(i\omega t)\dfrac{k_{SAW}}{k_\perp}\left(\dfrac{W_t \exp(i\varphi_z) - W_b \exp(-iHk_\perp)}{\sin(Hk_\perp)}\cos(zk_\perp) - iW_b \exp(-izk_\perp)\right)\sin(k_{SAW}x - \varphi_x)\right), \\ w_1 = Re\left(\exp(i\omega t)\left(\dfrac{W_t \exp(i\varphi_z) - W_b \exp(-iHk_\perp)}{\sin(Hk_\perp)}\sin(zk_\perp) + W_b \exp(-izk_\perp)\right)\cos(k_{SAW}x - \varphi_x)\right). \end{cases} \tag{2.41}$$

Likewise, the (y, z, t) subproblem described by boundary conditions in (2.10*b*) and (2.10*d*) can be solved in the same way. Superposing the 2-D sub-solutions gives the complete 3-D first-order velocity field

$$\begin{cases} u_1 = Re\left(\exp(i\omega t)\dfrac{k_{SAW}}{k_\perp}\left(\dfrac{W_t \exp(i\varphi_z) - W_b \exp(-iHk_\perp)}{\sin(Hk_\perp)}\cos(zk_\perp) - iW_b \exp(-izk_\perp)\right)\sin(k_{SAW}x - \varphi_x)\right), \\ v_1 = Re\left(\exp(i\omega t - i\varphi_\Delta)\dfrac{k_{SAW}}{k_\perp}\left(\dfrac{W_t \exp(i\varphi_z) - W_b \exp(-iHk_\perp)}{\sin(Hk_\perp)}\cos(zk_\perp) - iW_b \exp(-izk_\perp)\right)\right) \\ \qquad \cdot \sin(k_{SAW}y - \varphi_y), \\ w_1 = Re(\exp(i\omega t)\left(\dfrac{W_t \exp(i\varphi_z) - W_b \exp(-iHk_\perp)}{\sin(Hk_\perp)}\sin(zk_\perp) + W_b \exp(-izk_\perp)\right) \\ \qquad \cdot (\cos(k_{SAW}x - \varphi_x) + \exp(-i\varphi_\Delta)\cos(k_{SAW}y - \varphi_y))). \end{cases} \tag{2.42}$$

https://doi.org/10.1017/jfm.2026.11970 Published online by Cambridge University Press

The first-order pressure and density fields are obtained by substituting (2.42) into (2.4), as follows:

$$\begin{cases} p_1 = c^2 \rho_1, \\ \rho_1 = Re\Big(i \frac{\rho_0}{\omega} \exp(i\omega t) \Big(\frac{k_{SAW}^2}{k_\perp} + k_\perp \Big) \Big(\frac{W_t \exp(i\varphi_z) - W_b \exp(-iHk_\perp)}{\sin(Hk_\perp)} \cos(zk_\perp) - i W_b \exp(-izk_\perp) \Big) \\ \qquad \cdot (\cos(k_{SAW} x - \varphi_x) + \exp(-i\varphi_\Delta) \cos(k_{SAW} y - \varphi_y)) \Big). \end{cases} \tag{2.43}$$

2.7. *Second-order streaming field*

Following the perturbation method in § 2.2, substituting (2.3) into (2.1) and collecting the second-order terms yields the governing equations for the second-order response. In the present section, we focus on the quasi-steady acoustic streaming field, whose characteristic evolution time is much longer than the acoustic period of the SAW excitation. Therefore, the second-order equations are averaged over one acoustic period, and the variables $\boldsymbol{v}_2$, p_2 and ρ_2 hereafter denote the time-averaged second-order velocity, pressure and density fields, respectively. The governing equations are then obtained as

$$\begin{cases} \nabla p_2 - \mu \nabla^2 \boldsymbol{v}_2 - \Big(\mu_b + \dfrac{\mu}{3} \Big) \nabla (\nabla \cdot \boldsymbol{v}_2) = \left\langle -\rho_1 \dfrac{\partial v_1}{\partial t} - \rho_0 (\boldsymbol{v}_1 \cdot \nabla) \boldsymbol{v}_1 \right\rangle, \\ \rho_0 \nabla \cdot \boldsymbol{v}_2 = \langle -\nabla \cdot (\rho_1 \boldsymbol{v}_1) \rangle, \\ p_2 = c^2 \rho_2, \end{cases} \tag{2.44}$$

where the operator $\langle Q(t) \rangle$ denotes the time average of the variable $Q(t)$, i.e. $\langle Q(t) \rangle := (1/T) \int_t^{t+T} Q(t)\, \mathrm{d}t$. The boundary conditions are

$$\begin{cases} \boldsymbol{v}_2 (x, y, 0) = -\left\langle \big(\boldsymbol{\xi}_1 (x, y, 0) \cdot \nabla \big) \boldsymbol{v}_1 (x, y, 0) \right\rangle, \\ \boldsymbol{v}_2 (x, y, H) = -\left\langle \big(\boldsymbol{\xi}_1 (x, y, H) \cdot \nabla \big) \boldsymbol{v}_1 (x, y, H) \right\rangle, \end{cases} \tag{2.45}$$

where $\boldsymbol{\xi}_1(x, y, z) = \int \boldsymbol{v}_1(x, y, z) \mathrm{d}t$ denotes the acoustic displacement. Following the method introduced in § 2.4, (2.44) can be decomposed into a set of 2-D subproblems. Here, we present the representative (x, z) subproblem associated with the x-directional first-order field:

$$\begin{cases} \dfrac{\partial p_2}{\partial x} - \mu \left(\dfrac{\partial^2 u_2}{\partial x^2} + \dfrac{\partial^2 u_2}{\partial z^2} \right) - \Big(\mu_b + \dfrac{\mu}{3} \Big) \dfrac{\partial}{\partial x} \left(\dfrac{\partial u_2}{\partial x} + \dfrac{\partial w_2}{\partial z} \right) = \left\langle -\rho_1 \dfrac{\partial u_1}{\partial t} - \rho_0 \left(u_1 \dfrac{\partial u_1}{\partial x} + w_1 \dfrac{\partial u_1}{\partial z} \right) \right\rangle, \\ \dfrac{\partial p_2}{\partial z} - \mu \left(\dfrac{\partial^2 w_2}{\partial x^2} + \dfrac{\partial^2 w_2}{\partial z^2} \right) - \Big(\mu_b + \dfrac{\mu}{3} \Big) \dfrac{\partial}{\partial z} \left(\dfrac{\partial u_2}{\partial x} + \dfrac{\partial w_2}{\partial z} \right) = \left\langle -\rho_1 \dfrac{\partial w_1}{\partial t} - \rho_0 \left(u_1 \dfrac{\partial w_1}{\partial x} + w_1 \dfrac{\partial w_1}{\partial z} \right) \right\rangle, \\ \rho_0 \left(\dfrac{\partial u_2}{\partial x} + \dfrac{\partial w_2}{\partial z} \right) = \left\langle -\dfrac{\partial (\rho_1 u_1)}{\partial x} - \dfrac{\partial (\rho_1 w_1)}{\partial z} \right\rangle. \end{cases} \tag{2.46}$$

https://doi.org/10.1017/jfm.2026.11970 Published online by Cambridge University Press

We first consider the inhomogeneous terms in (2.46). According to (2.31) and (2.32)

$$\begin{cases} u_1 = Re\,(\tilde{u}_1) = \dfrac{\tilde{u}_1 + \tilde{u}_1^*}{2}, \\ w_1 = Re\,(\tilde{w}_1) = \dfrac{\tilde{w}_1 + \tilde{w}_1^*}{2}, \\ \rho_1 = Re\,(\tilde{\rho}_1) = \dfrac{\tilde{\rho}_1 + \tilde{\rho}_1^*}{2}, \end{cases} \tag{2.47a}$$

where Q^* denotes the complex conjugate of Q

$$\begin{cases} \tilde{u}_1 = \exp(i\omega t) \cdot \sin(k_{SAW}x - \varphi_x) \cdot \sum_{j=1,2,3,4} G_j^u \exp(\lambda_j z), \\ \tilde{w}_1 = \exp(i\omega t) \cdot \cos(k_{SAW}x - \varphi_x) \cdot \sum_{j=1,2,3,4} G_j^w \exp(\lambda_j z), \\ \tilde{\rho}_1 = \exp(i\omega t) \cdot \cos(k_{SAW}x - \varphi_x) \cdot \sum_{j=1,2,3,4} G_j^\rho \exp(\lambda_j z), \end{cases} \tag{2.47b}$$

where G_j^u, G_j^w and G_j^ρ are constants independent of (x, y, z, t). Similarly, all quantities denoted by G_j^q in § 2.7 are constants obtained from (2.31) and (2.32) and are independent of (x, y, z, t). Noting that $\langle \exp(i\omega t) \exp(i\omega t) \rangle = 0$ and $\langle \exp(i\omega t) \exp(-i\omega t) \rangle = 1$, the inhomogeneous terms in (2.46) can be reorganised into products of functions depending only on x and z, respectively, i.e.

$$\begin{cases} \left\langle -\rho_1 \dfrac{\partial u_1}{\partial t} - \rho_0 \left(u_1 \dfrac{\partial u_1}{\partial x} + w_1 \dfrac{\partial u_1}{\partial z} \right) \right\rangle = \dfrac{1}{8} \sin\,(2k_{SAW}x - 2\varphi_x)\, F_{1,s}^{inh}(z), \\ \left\langle -\rho_1 \dfrac{\partial w_1}{\partial t} - \rho_0 \left(u_1 \dfrac{\partial w_1}{\partial x} + w_1 \dfrac{\partial w_1}{\partial z} \right) \right\rangle = \dfrac{1}{8} \cos\,(2k_{SAW}x - 2\varphi_x)\, F_{2,\mathrm{c}}^{inh}(z) + \dfrac{1}{8} F_{2,0}^{inh}(z), \\ \left\langle -\dfrac{\partial\,(\rho_1 u_1)}{\partial x} - \dfrac{\partial\,(\rho_1 w_1)}{\partial z} \right\rangle = \dfrac{1}{8} \cos\,(2k_{SAW}x - 2\varphi_x)\, F_{3,\mathrm{c}}^{inh}(z) + \dfrac{1}{8} F_{3,0}^{inh}(z), \end{cases} \tag{2.48}$$

where $F_{j,\mathrm{s}}^{inh}(z)$, $F_{j,\mathrm{c}}^{inh}(z)$ and $F_{j,0}^{inh}(z)$ are real functions of z and can be written as sums of exponential functions. The subscripts 's', 'c' and '0' indicate that the corresponding x-dependent factors are sine, cosine and constant terms, respectively. Similarly, all quantities denoted by $F_j^q(z)$in this section are functions of z obtained from (2.31) and (2.32). The boundary conditions in (2.45) can be written in the same form as (2.48), i.e.

$$\begin{cases} u_2\,(x, 0) = \dfrac{1}{8} \sin\,(2k_{SAW}x - 2\varphi_x)\, F_{1,s}^{bond}(0), \\ u_2\,(x, H) = \dfrac{1}{8} \sin\,(2k_{SAW}x - 2\varphi_x)\, F_{1,s}^{bond}(H), \\ w_2\,(x, 0) = \dfrac{1}{8} \left(\cos\,(2k_{SAW}x - 2\varphi_x)\, F_{1,\mathrm{c}}^{bond}(0) + F_{1,0}^{bond}(0) \right), \\ w_2\,(x, H) = \dfrac{1}{8} \left(\cos\,(2k_{SAW}x - 2\varphi_x)\, F_{1,\mathrm{c}}^{bond}(H) + F_{1,0}^{bond}(H) \right). \end{cases} \tag{2.49}$$

https://doi.org/10.1017/jfm.2026.11970 Published online by Cambridge University Press

Since both the inhomogeneous terms in (2.48) and the boundary conditions in (2.49) are separable, the same method as that used in § 2.5 can be adopted, i.e.

$$\begin{cases} \tilde{u}_2 = \tilde{U}_{2,+}(z)\exp\left(i\ (2k_{SAW}x - 2\varphi_x)\right) + \tilde{U}_{2,-}(z)\exp\left(i\ (-2k_{SAW}x + 2\varphi_x)\right) + \tilde{U}_{2,0}, \\ \tilde{w}_2 = \tilde{W}_{2,+}(z)\exp\left(i\ (2k_{SAW}x - 2\varphi_x)\right) + \tilde{W}_{2,-}(z)\exp\left(i\ (-2k_{SAW}x + 2\varphi_x)\right) + \tilde{W}_{2,0}, \\ \tilde{p}_2 = \tilde{P}_{2,+}(z)\exp\left(i\ (2k_{SAW}x - 2\varphi_x)\right) + \tilde{P}_{2,-}(z)\exp\left(i\ (-2k_{SAW}x + 2\varphi_x)\right) + \tilde{P}_{2,0}. \end{cases} \tag{2.50}$$

Taking the component in (2.50) that contains the factor $\exp(i(2k_{SAW}x - 2\varphi_x))$, the differential operators in (2.46) are applied in their frequency-domain form, with $(\partial/\partial x) = 2ik_{SAW}$ and $(\partial/\partial z) = (\mathrm{d}/\mathrm{d}z)$, respectively. Therefore, (2.46) can be reduced to a set of linear inhomogeneous ODEs in z

$$2ik_{SAW}\tilde{P}_{2,+}(z) - \mu\frac{\mathrm{d}^2\tilde{U}_{2,+}(z)}{\mathrm{d}z^2} + \left(\mu_b + \frac{4\mu}{3}\right)4k_{SAW}^2\tilde{U}_{2,+}(z) - 2i\left(\mu_b + \frac{\mu}{3}\right)k_{SAW}\frac{\mathrm{d}\tilde{W}_{2,+}(z)}{\mathrm{d}z} = F_{1,+}^{inh}(z), \tag{2.51a}$$

$$\frac{\mathrm{d}\tilde{P}_{2,+}(z)}{\mathrm{d}z} + 4\mu k_{SAW}^2\tilde{W}_{2,+}(z) - 2i\left(\mu_b + \frac{\mu}{3}\right)k_{SAW}\frac{\mathrm{d}\tilde{U}_{2,+}(z)}{\mathrm{d}z} - \left(\mu_b + \frac{4\mu}{3}\right)\frac{\mathrm{d}^2\tilde{W}_{2,+}(z)}{\mathrm{d}z^2} = F_{2,+}^{inh}(z), \tag{2.51b}$$

$$\rho_0\left(2ik_{SAW}\tilde{U}_{2,+}(z) + \frac{\mathrm{d}\tilde{W}_{2,+}(z)}{\mathrm{d}z}\right) = F_{3,+}^{inh}(z), \tag{2.51c}$$

where

$$\begin{cases} F_{1,+}^{inh}(z) = -\dfrac{i}{16}\displaystyle\sum_{\substack{m=1,2,3,4 \\ n=1,2,3,4}} G_{mn,1}^{inh}\exp\left(\left(\lambda_m^* + \lambda_n\right)z\right), \\ F_{2,+}^{inh}(z) = \dfrac{1}{16}\displaystyle\sum_{\substack{m=1,2,3,4 \\ n=1,2,3,4}} G_{mn,2}^{inh}\exp\left(\left(\lambda_m^* + \lambda_n\right)z\right), \\ F_{3,+}^{inh}(z) = \dfrac{1}{16}\displaystyle\sum_{\substack{m=1,2,3,4 \\ n=1,2,3,4}} G_{mn,3}^{inh}\exp\left(\left(\lambda_m^* + \lambda_n\right)z\right). \end{cases} \tag{2.51d}$$

The corresponding boundary conditions are

$$\begin{cases} \tilde{U}_{2,+}(0) = -\dfrac{i}{16}F_{1,s}^{bond}(0), \\ \tilde{U}_{2,+}(H) = -\dfrac{i}{16}F_{1,s}^{bond}(H), \\ \tilde{W}_{2,+}(0) = \dfrac{1}{16}F_{1,\mathrm{c}}^{bond}(0), \\ \tilde{W}_{2,+}(H) = \dfrac{1}{16}F_{1,\mathrm{c}}^{bond}(H). \end{cases} \tag{2.52}$$

From (2.51c), we obtain

$$\tilde{U}_{2,+}(z) = \frac{1}{2ik_{SAW}}\left(\frac{F_{3,+}^{inh}(z)}{\rho_0} - \frac{\mathrm{d}\tilde{W}_{2,+}(z)}{\mathrm{d}z}\right). \tag{2.53}$$

https://doi.org/10.1017/jfm.2026.11970 Published online by Cambridge University Press

Substituting (2.53) into (2.51*a*) gives

$$\tilde{P}_{2,+}(z)=\frac{\mu}{4k_{SAW}^2}\frac{d^3\tilde{W}_{2,+}(z)}{dz^3}-\mu\frac{\mathrm{d}\tilde{W}_{2,+}(z)}{\mathrm{d}z}+\frac{F_{1,+}^{inh}(z)}{2ik_{SAW}}-\frac{\mu}{4\rho_0k_{SAW}^2}\frac{d^2F_{3,+}^{inh}(z)}{dz^2}+\left(\mu_b+\frac{4\mu}{3}\right)\frac{F_{3,+}^{inh}(z)}{\rho_0}. \tag{2.54}$$

Substituting (2.53) and (2.54) into (2.51*b*) gives

$$\left(\frac{\mathrm{d}^2}{\mathrm{d}z^2}-4k_{SAW}^2\right)^2\tilde{W}_{2,+}(z)=S(z), \tag{2.55a}$$

where the inhomogeneous term is

$$S(z)=\frac{2ik_{SAW}}{\mu}\frac{\mathrm{d}F_{1,+}^{inh}(z)}{\mathrm{d}z}+\frac{4k_{SAW}^2}{\mu}F_{2,+}^{inh}(z)+\frac{1}{\rho_0}\frac{\mathrm{d}^3F_{3,+}^{inh}(z)}{\mathrm{d}z^3}-\frac{4k_{SAW}^2}{\rho_0}\frac{\mathrm{d}F_{3,+}^{inh}(z)}{\mathrm{d}z}. \tag{2.55b}$$

The characteristic equation of the homogeneous part of (2.55*a*) has two double roots. Thus, the homogeneous solution is

$$\tilde{W}_{2,+}^{hom}(z)=\left(C_{+,1}^{hom}+zC_{+,2}^{hom}\right)\exp\left(2k_{SAW}z\right)+\left(C_{+,3}^{hom}+zC_{+,4}^{hom}\right)\exp\left(-2k_{SAW}z\right). \tag{2.56}$$

According to (2.51*d*), the inhomogeneous term in (2.55*b*) can be written as

$$S(z)=\sum_{\substack{m=1,2,3,4\\n=1,2,3,4}}S_{mn}\exp(s_{mn}z), \tag{2.57a}$$

where

$$\begin{cases}S_{mn}=\dfrac{1}{16}\left(\dfrac{2k_{SAW}s_{mn}}{\mu}G_{mn,1}^{inh}+\dfrac{4k_{SAW}^2}{\mu}G_{mn,2}^{inh}+\dfrac{s_{mn}^3-4k_{SAW}^2s_{mn}}{\rho_0}G_{mn,3}^{inh}\right)\\ s_{mn}=\lambda_m^*+\lambda_n.\end{cases} \tag{2.57b}$$

The corresponding particular solution for inhomogeneous part is

$$\tilde{W}_{2,+}^{inh}(z)=\sum_{\substack{m=1,2,3,4\\n=1,2,3,4}}\frac{S_{mn}}{\left(s_{mn}^2-4k_{SAW}^2\right)^2}\exp\left(s_{mn}z\right). \tag{2.58}$$

Therefore, the general solution of $\tilde{W}_{2,+}(z)$ is

$$\tilde{W}_{2,+}(z)=\tilde{W}_{2,+}^{hom}(z)+\tilde{W}_{2,+}^{inh}(z)=\left(C_{+,1}^{hom}+zC_{+,2}^{hom}\right)\exp\left(2k_{SAW}z\right)+\left(C_{+,3}^{hom}+zC_{+,4}^{hom}\right)\exp(-2k_{SAW}z)+\sum_{\substack{m=1,2,3,4\\n=1,2,3,4}}\frac{S_{mn}}{\left(s_{mn}^2-4k_{SAW}^2\right)^2}\exp(s_{mn}z). \tag{2.59}$$

From (2.53) and (2.54), $\tilde{U}_{2,+}(z)$ and $\tilde{P}_{2,+}(z)$ can be obtained. To determine the homogeneous coefficients $C_{+,j}^{hom}$, substituting (2.53) into the boundary conditions in (2.52)

https://doi.org/10.1017/jfm.2026.11970 Published online by Cambridge University Press

yields

$$\begin{cases} \dfrac{\mathrm{d}\tilde{W}_{2,+}(0)}{\mathrm{d}z} = \dfrac{F_{3,+}^{inh}(0)}{\rho_0} - \dfrac{k_{SAW}}{8} F_{1,s}^{bond}(0), \\ \dfrac{\mathrm{d}\tilde{W}_{2,+}(H)}{\mathrm{d}z} = \dfrac{F_{3,+}^{inh}(H)}{\rho_0} - \dfrac{k_{SAW}}{8} F_{1,s}^{bond}(H), \\ \tilde{W}_{2,+}(0) = \dfrac{1}{16} F_{1,\mathrm{c}}^{bond}(0), \\ \tilde{W}_{2,+}(H) = \dfrac{1}{16} F_{1,\mathrm{c}}^{bond}(H). \end{cases} \tag{2.60}$$

Substituting (2.59) into (2.60) gives

$$\boldsymbol{M}_{\mathrm{bond}} \begin{bmatrix} C_{+,1}^{hom} \\ C_{+,2}^{hom} \\ C_{+,3}^{hom} \\ C_{+,4}^{hom} \end{bmatrix} = \begin{bmatrix} \dfrac{F_{3,+}^{inh}(0)}{\rho_0} - \dfrac{k_{SAW}}{8} F_{1,s}^{bond}(0) - \sum\limits_{\substack{m=1,2,3,4 \\ n=1,2,3,4}} \dfrac{s_{mn} S_{mn}}{\left(s_{mn}^2 - 4k_{SAW}^2\right)^2} \\ \dfrac{F_{3,+}^{inh}(H)}{\rho_0} - \dfrac{k_{SAW}}{8} F_{1,s}^{bond}(H) - \sum\limits_{\substack{m=1,2,3,4 \\ n=1,2,3,4}} \dfrac{s_{mn} S_{mn}}{\left(s_{mn}^2 - 4k_{SAW}^2\right)^2} \exp\left(s_{mn} H\right) \\ \dfrac{1}{16} F_{1,\mathrm{c}}^{bond}(0) - \sum\limits_{\substack{m=1,2,3,4 \\ n=1,2,3,4}} \dfrac{S_{mn}}{\left(s_{mn}^2 - 4k_{SAW}^2\right)^2} \\ \dfrac{1}{16} F_{1,\mathrm{c}}^{bond}(H) - \sum\limits_{\substack{m=1,2,3,4 \\ n=1,2,3,4}} \dfrac{S_{mn}}{\left(s_{mn}^2 - 4k_{SAW}^2\right)^2} \exp\left(s_{mn} H\right) \end{bmatrix}, \tag{2.61a}$$

where

$$\boldsymbol{M}_{bond} = \begin{bmatrix} 2k_{SAW} & 1 & -2k_{SAW} & 1 \\ 2k_{SAW} \exp\left(2k_{SAW} H\right) & \left(1 + 2Hk_{SAW}\right) \exp\left(2k_{SAW} H\right) & -2k_{SAW} \exp\left(-2k_{SAW} H\right) & \left(1 - 2Hk_{SAW}\right) \exp\left(-2k_{SAW} H\right) \\ 1 & 0 & 1 & 0 \\ \exp\left(2k_{SAW} H\right) & H \exp\left(2k_{SAW} H\right) & \exp\left(-2k_{SAW} H\right) & H \exp\left(-2k_{SAW} H\right) \end{bmatrix}. \tag{2.61b}$$

For the component in (2.50) containing the factor $\exp(-i(2k_{SAW}x - 2\varphi_x))$, repeating (2.51)–(2.61) gives

$$\begin{cases} \tilde{U}_{2,+}(z) = -\tilde{U}_{2,-}(z), \\ \tilde{W}_{2,+}(z) = \tilde{W}_{2,-}(z). \end{cases} \tag{2.62}$$

Similarly, for the spatially uniform components $\tilde{U}_{2,0}(z)$, $\tilde{W}_{2,0}(z)$ and $\tilde{P}_{2,0}(z)$, the operators become $(\partial/\partial x) = 0$ and $(\partial/\partial z) = (\mathrm{d}/\mathrm{d}z)$. Therefore, the following linear

https://doi.org/10.1017/jfm.2026.11970 Published online by Cambridge University Press

inhomogeneous ODEs in the z-direction are obtained:

$$\begin{cases} -\mu \dfrac{\mathrm{d}^2 \tilde{U}_{2,0}(z)}{\mathrm{d}z^2} = 0, & (2.63a) \\ \dfrac{\mathrm{d}\tilde{P}_{2,0}(z)}{\mathrm{d}z} - \left(\mu_b + \dfrac{4\mu}{3}\right) \dfrac{\mathrm{d}^2 \tilde{W}_{2,0}(z)}{\mathrm{d}z^2} = F_{2,0}^{inh}(z), & (2.63b) \\ \rho_0 \dfrac{\mathrm{d}\tilde{W}_{2,0}(z)}{\mathrm{d}z} = F_{3,0}^{inh}(z), & (2.63c) \end{cases}$$

where

$$\begin{cases} F_{2,0}^{inh}(z) = \dfrac{1}{8} \sum\limits_{\substack{m=1,2,3,4 \\ n=1,2,3,4}} G_{mn,2,0}^{inh} \exp\left(\left(\lambda_m^* + \lambda_n\right) z\right) \\ F_{3,0}^{inh}(z) = \dfrac{1}{8} \sum\limits_{\substack{m=1,2,3,4 \\ n=1,2,3,4}} G_{mn,3,0}^{inh} \exp\left(\left(\lambda_m^* + \lambda_n\right) z\right). \end{cases} \quad (2.63d)$$

Solving (2.63) with the corresponding boundary conditions gives

$$\begin{cases} \tilde{U}_{2,0}(z) = 0 \\ \tilde{W}_{2,0}(z) = \dfrac{1}{8} F_{1,0}^{bond}(0) + \dfrac{1}{8} \sum\limits_{\substack{m=1,2,3,4 \\ n=1,2,3,4}} \dfrac{G_{mn,3,0}^{inh}}{\rho_0 \left(\lambda_m^* + \lambda_n\right)} \left(\exp\left(\left(\lambda_m^* + \lambda_n\right) z\right) - 1\right). \end{cases} \quad (2.64)$$

Combining the results in (2.50) with (2.59), (2.62) and (2.64), we obtain the second-order solution for the (x, z) subproblem

$$\begin{aligned} \tilde{w}_2 = 2 \left(\cos\left(2k_{SAW}x - 2\varphi_x\right)\right) & \left(\left(C_{+,1}^{hom} + zC_{+,2}^{hom}\right) \exp\left(2k_{SAW}z\right)\right. \\ & + \left(C_{+,3}^{hom} + zC_{+,4}^{hom}\right) \exp\left(-2k_{SAW}z\right) \\ & + \sum_{\substack{m=1,2,3,4 \\ n=1,2,3,4}} \frac{S_{mn}}{\left(s_{mn}^2 - 4k_{SAW}^2\right)^2} \exp\left(s_{mn}z\right) \Big) + \frac{1}{8} F_{1,0}^{bond}(0) \\ & + \frac{1}{8} \sum_{\substack{m=1,2,3,4 \\ n=1,2,3,4}} \frac{G_{mn,3,0}^{inh}}{\left(\lambda_m^* + \lambda_n\right) \rho_0} \left(\exp\left(\left(\lambda_m^* + \lambda_n\right) z\right) - 1\right), \end{aligned} \quad (2.65a)$$

and

$$\begin{aligned} \tilde{u}_2 = \frac{\sin\left(2k_{SAW}x - 2\varphi_x\right)}{k_{SAW}} & \left(\frac{F_{3,+}^{inh}(z)}{\rho_0} - \left(2k_{SAW}C_{+,1}^{hom} + C_{+,2}^{hom} + 2zk_{SAW}C_{+,2}^{hom}\right) \right. \\ & \exp\left(2k_{SAW}z\right) - \left(-2k_{SAW}C_{+,3}^{hom} + C_{+,4}^{hom} - 2zk_{SAW}C_{+,4}^{hom}\right) \exp\left(-2k_{SAW}z\right) \\ & \left. - \sum_{\substack{m=1,2,3,4 \\ n=1,2,3,4}} \frac{s_{mn}S_{mn}}{\left(s_{mn}^2 - 4k_{SAW}^2\right)^2} \exp\left(s_{mn}z\right) \right). \end{aligned} \quad (2.65b)$$

https://doi.org/10.1017/jfm.2026.11970 Published online by Cambridge University Press

The physical time-averaged second-order velocity field is obtained by taking the real part of (2.65).

3. Validation and discussion

In this section, we validate the proposed theoretical framework and examine the role of the fluid viscosity in detail. Section 3.1 demonstrates the consistency between the theoretical and finite-element simulation results of the first-order acoustic velocity field. Section 3.2 presents the profiles of characteristic acoustic fields for $\varphi_\Delta = \pi/2$ and $\varphi_\Delta = 0$, whose nodal surface geometries are determined from both theoretical predictions and numerical simulation and were also observed from experiments of Bernard *et al.* (2017). In § 3.3, we particularly focus on the pressure nodal positions along out-of-plane direction (z-direction) formed in the dual-side-actuated acoustofluidic system. Lastly, the influence of the viscosity on the resulting acoustofluidic field is analysed in § 3.4.

To compare analytical solutions with numerical results, we establish a 3-D numerical model based on the finite-element method. For simulations involving liquid water, material properties of $\rho_0 = 998.2\ \mathrm{kg\ m^{-3}}$, $c = 1481.4\ \mathrm{m\ s^{-1}}$, $\mu = 1.0093\ \mathrm{mPa\ s}$, $\mu_B = 2.8161\ \mathrm{mPa\ s}$ were employed (Li *et al.* 2025*a*). Following the requirements for periodic boundary conditions described in § 2.3, the SAW wavelength λ_{SAW} is set to 300 μm, resulting in a wavenumber $k_{SAW} = 2\pi/\lambda_{SAW} = 20944\ \mathrm{m^{-1}}$. Lithium niobate ($LiNbO_3$), a commonly used piezoelectric substrate material, has a Rayleigh wave velocity of $c_{SAW} = 3994\ \mathrm{m\ s^{-1}}$. Therefore, the IDT excitation frequency is set to $f = c_{SAW}/\lambda_{SAW} = 13.3$ MHz.

3.1. *First-order velocity field*

In § 3.1, the computational domain is defined as a cubic fluid region with a square base length L of $\lambda_{SAW} = 300\ \mu\mathrm{m}$ and a height H of 50 μm, resulting in 62 450 mesh nodes in the region of interest. The acoustic velocity and pressure fields within the fluid are simulated using thermoviscous acoustics, a frequency-domain interface and the total number of degrees of freedom (DOFs) in the 3-D frequency-domain simulations is 484,315. A higher DOF generally indicates increased computational cost. To ensure generality, the acoustic field depicted in figure 4 was chosen with parameters $(W_b/\omega) = 1$ nm, $(W_t/\omega) = -0.7$ nm, $\varphi_x = (\pi/2) + 1$ and $\varphi_y = (\pi/2)$. Applying these parameters, figures 4(*a*) and 4(*b*) show the structure of representative acoustofluidic fields with $\varphi_\Delta = \pi/2$ and $\varphi_\Delta = 0$, respectively.

Due to the low viscosity of liquid water, the viscous effect is limited to a very narrow region within the boundary layers, which is detailed in § 3.4. The viscous effect outside of the boundary layers, however, is negligible. Therefore, in most region, the theoretical calculations using (2.31) closely matched the results obtained by the inviscid solution in (2.42). Therefore, we hereby employ the inviscid formula (2.42) to calculate the acoustic field within water, and we present the analytical results of the z-direction velocity component w_1 in figure 4. To validate the theoretical results from our 3-D numerical model, we specifically calculate the magnitude of w_1 along three cutlines in the x-, y- and z- directions, as shown in figure 4. The black lines in figure 4 represent the theoretically calculated w_1 magnitude along these intersecting cutlines, while the red cross markers denote the simulation data at each node position.

To assess the agreement between theoretical and numerical results, we employed the coefficient of determination R^2, which quantifies the degree to which a theoretical framework accounts for the variability in the numerical data. An R^2 value of 1 indicates a perfect fit between the theoretical model and the numerical data, while $R^2 = 0$ implies that the theoretical model performs no better than simply predicting the mean of the

https://doi.org/10.1017/jfm.2026.11970 Published online by Cambridge University Press

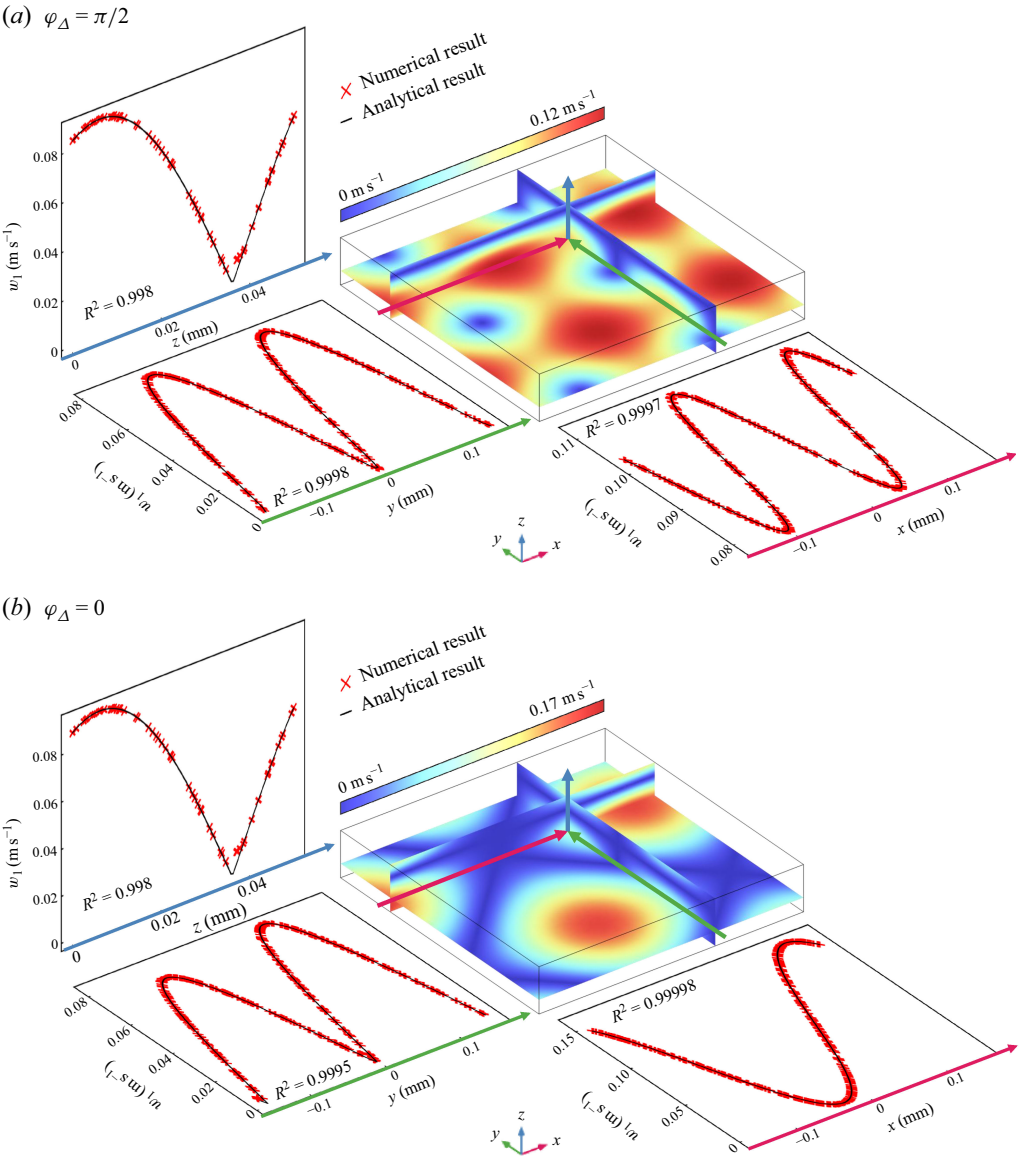


Figure 4. Characteristic first-order acoustic velocity fields for (*a*) $\varphi_\Delta = \pi/2$ and (*b*) $\varphi_\Delta = 0$. Comparison between theory and finite-element simulation is conducted along three characteristic cutlines in the principal coordinate directions. Red crosses mark the simulated values at computational grid nodes along these cutlines, and the black solid lines represent the analytical prediction.

numerical data. The coefficient R^2 is computed using the Numpy 2.0.0 lib in Python 3.10.15. For the two characteristic acoustic fields in figure 4, the R^2 value consistently exceeds 0.99. The two cases with lowest R^2 values appear in the profiles of w_1 along the z-axis, where $R^2 = 0.998$. The slight discrepancy observed near the minimum w_1 magnitude at $z = 40\,\mu\text{m}$ is attributed to the relatively coarse computational mesh resolution in this region, which causes the abrupt changes in the w_1 magnitude not captured as accurately as in other cases. Nevertheless, an assessment of $R^2 = 0.998$ still indicates high reliability of the theoretical framework. All other comparisons along the x- and y- directions yield

https://doi.org/10.1017/jfm.2026.11970 Published online by Cambridge University Press

R^2 values greater than 0.999, demonstrating that the theoretical calculations accurately represent the numerical simulation results and significantly reduce computational cost for similar scenarios. Additional comparisons for the pressure field, the other velocity components and the viscous analytical formulation against thermoviscous simulations are provided in Appendix A, where similarly good agreement is observed.

It is noteworthy that the velocity distributions shown in figure 4 exhibit similar profiles along the z direction yet display distinct periodicities along the x and y directions. For a phase difference $\varphi_\Delta = \pi/2$ (figure 4*a*), the velocity field within the square domain of side length $L = \lambda_{SAW}$ exhibits two pairs of peaks and valleys along both the x and y axes, indicating a spatial periodicity of $\lambda_{SAW}/2$ in these directions. In contrast, for $\varphi_\Delta = 0$ (figure 4*b*), the velocity distribution shows only one peak–trough pair along x axis and two peaks of different magnitudes along the y axis, corresponding to a periodicity of λ_{SAW} along both axes. These contrasting acoustic field patterns and the associated arrangements of PNs enable distinct microfluidic functionalities (Ding *et al.* 2012; Melde *et al.* 2016). Accordingly, § 3.2 presents a quantitative and qualitative analysis of the acoustic field shape and nodal positions for $\varphi_\Delta = \pi/2$ and $\varphi_\Delta = 0$.

3.2. *Geometry of nodal surface*

In typical applications of acoustofluidic particle manipulation, particles suspended in the liquid migrate towards either PNs or ANs based on their acoustic contrast factor (Baudoin & Thomas 2020). In this section, we analyse the spatial locations of PNs within the 3-D standing-wave field using the inviscid analytical solutions given in (2.43). To determine the position of PNs, we identify the locations where the complex amplitude of the first-order pressure field vanishes in (2.43), which yields

$$\begin{cases} 0 = f_1\,(x,\,y)\cdot f_2(z), \\ f_1\,(x,\,y) = \cos\,(k_{SAW}x - \varphi_x) + \exp\,(-i\varphi_\Delta)\cos\left(k_{SAW}y - \varphi_y\right), \\ f_2(z) = \dfrac{W_t\exp\,(i\varphi_z) - W_b\exp\,(-iHk_\perp)}{\sin\,(Hk_\perp)}\cos\,(zk_\perp) - iW_b\exp\,(-izk_\perp). \end{cases} \tag{3.1}$$

Equation (3.1) describes the pressure nodal surfaces within the 3-D acoustic field. The equation factorises into two independent components: a lateral term $f_1(x,\,y)$ depending only on the x- and y-coordinates, and a vertical term $f_2(z)$ depending only on the z-coordinate. This decomposition indicates that the full 3-D pressure nodal surface can be understood as the combination of two independent nodal surface systems. Setting $f_1(x,\,y)$ or $f_2(z)$ in (3.1) to zero yields the conditions for the two pressure nodal surface systems. Specifically, the condition $f_1(x,\,y) = 0$ yields pressure nodal surfaces that are parallel to the z-axis, while the surface defined by $f_2(z) = 0$ forms planar pressure nodal surfaces perpendicular to the z-axis. Considering the distinctive behaviour of the pressure nodal surface in the z-direction for a dual-side-actuated acoustofluidic system, a detailed analysis of the planar nodal positions defined by $f_2(z) = 0$ will be presented in § 3.3.

The pressure nodal surface system parallel to the z-axis exhibits a more complex structure. When $\varphi_\Delta = \pi/2$, the PN condition $f_1(x,\,y) = 0$ becomes

$$\cos\,(k_{SAW}x - \varphi_x) + i\cos\left(k_{SAW}y - \varphi_y\right) = 0, \tag{3.2}$$

which holds only when $\cos(k_{SAW}x - \varphi_x) = 0$ and $\cos(k_{SAW}y - \varphi_y) = 0$. This yields the family of solutions

https://doi.org/10.1017/jfm.2026.11970 Published online by Cambridge University Press

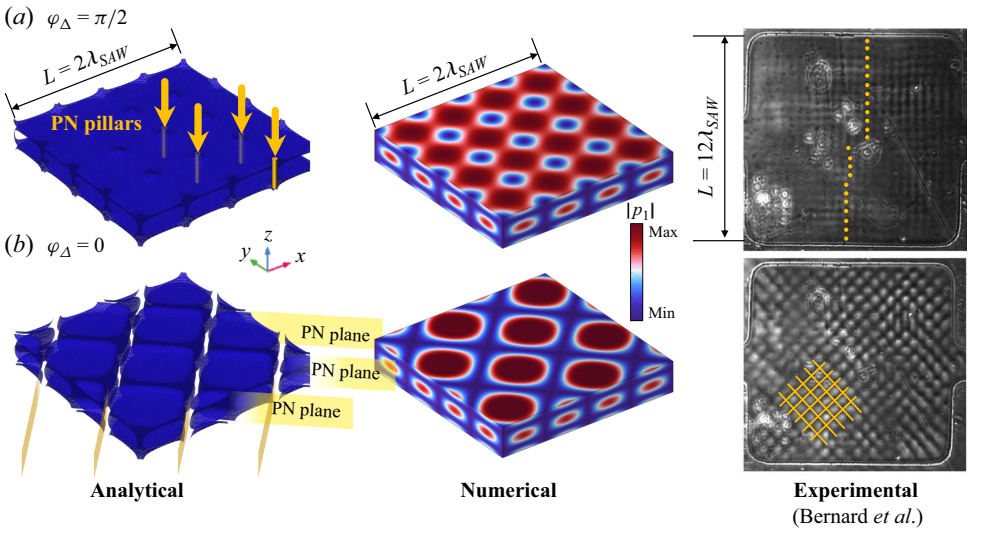


Figure 5. Characteristic first-order pressure fields for (*a*) $\varphi_\Delta = \pi/2$ and (*b*) $\varphi_\Delta = 0$. Each column shows, from left to right: the analytical pressure isosurface ($|p_1| = 0.1|p_1|_{max}$), the numerical pressure field and the top-view phase-contrast micrograph of the corresponding flow field reproduced from Bernard *et al.* (2017). The analytical and computational domains have a lateral dimension of $L = 2\lambda_{SAW}$ and a height of $H = \lambda_{SAW}/3$. In Bernard *et al.* (2017), the experimental set-up uses $L = 12\lambda_{SAW}$. Yellow cylinders and dots highlight the vertically oriented pressure nodal columns parallel to the z-axis. Semi-transparent yellow planes and solid grid lines indicate the nodal planes parallel to the z axis.

$$\begin{cases} x = \dfrac{\left(n + \dfrac{1}{2}\right)\pi + \varphi_x}{k_{SAW}}, \\ y = \dfrac{\left(m + \dfrac{1}{2}\right)\pi + \varphi_y}{k_{SAW}}, \end{cases} \quad n, m \in \mathbb{Z}, \tag{3.3}$$

indicating that, for $\varphi_\Delta = \pi/2$, the PNs form a lattice of columns parallel to the z-axis, each separated by a distance of $\pi/k_{SAW} = \lambda_{SAW}/2$. This conclusion is consistent with the results in figure 5(*a*), where the three columns from left to right show the low-pressure isosurface computed by (2.43), the pressure distribution obtained from numerical simulations and the experimentally observed flow field, respectively. As depicted in the left column of figure 5(*a*), these PN columns are denoted by the orange cylinders, while planar pressure nodal surfaces can also be observed perpendicular to the z-direction. The simulations likewise reveal that the nodal surfaces parallel to the z-axis form uniformly spaced columns with a periodicity of $\lambda_{SAW}/2$. Although the experimental image shows slightly distorted and vague nodal patterns near the sidewalls, the PNs at the central region of the fluid cavity retains equidistant, and the overall acoustic field preserves the same lattice structure as in analytical and numerical results. Notably, because this acoustic field configuration does not produce continuous nodal lines along both the x- and y-directions, it is particularly well suited for in-plane acoustofluidic particle manipulation, where particles can be rapidly and reliably trapped at these nodal columns to enable precise in-plane (x- and y- directional) control (Shen *et al.* 2024).

https://doi.org/10.1017/jfm.2026.11970 Published online by Cambridge University Press

When $\varphi_\Delta = 0$, (3.1) generates a different family of pressure nodal surfaces parallel to the z-axis, expressed as

$$\cos\left(k_{SAW}x - \varphi_x\right) + \cos\left(k_{SAW}y - \varphi_y\right) = 0. \tag{3.4}$$

The sufficient and necessary condition for (3.4) to hold is

$$\pm\left(y - \frac{\varphi_y}{k_{SAW}}\right) = x - \frac{\varphi_x}{k_{SAW}} + \frac{(2n+1)\,\pi}{k_{SAW}}, \quad n \in \mathbb{Z}. \tag{3.5}$$

As shown in figure 5(*b*), for $\varphi_\Delta = 0$, the resulting pressure field features two orthogonal sets of PN planes parallel to the z-axis, and each is oriented at an angle of 45 degrees to the x- and y- axes. The same pair of orthogonally intersecting surface systems are also observed in both simulations and experiments. Since the pressure gradient vanishes within each pressure nodal surface, for the applications of acoustofluidic particle manipulation, particles under this acoustic field are attracted to these nodal surfaces and cease to move. Therefore, precise trapping of particles at a specific point within the XY plane becomes challenging, and this acoustic field is generally avoided for in-plane (x- and y- directional) particle manipulation.

Equations (3.3) and (3.5) further demonstrate that the in-plane position (x, y) of the PNs can be independently tuned by adjusting (φ_x, φ_y). Specifically, small modifications $(\Delta\varphi_x, \Delta\varphi_y)$ to the IDT actuation phases lead to corresponding shifts in nodal position given by $(\Delta x, \Delta y) = (\Delta\varphi_x/k_{SAW}, \Delta\varphi_y/k_{SAW})$. This provides the theoretical basis for x- and y- directional acoustic manipulation, as demonstrated in Shen *et al.* (2024). Notably, since only $f_1(x, y)$ in (3.1) depends on (φ_x, φ_y), tuning the XY-plane nodal positions via phase (φ_x, φ_y) adjustments does not affect the nodal surfaces in the z-direction. Conversely, adjustments to the z-axis nodal-plane positions based on $f_2(z)$ do not affect the PN positions in the XY plane. Consequently, the pressure nodal surfaces in this acoustofluidic system can be independently controlled along all three spatial directions. In practical device design, this controllability is most reliably realised in the central working region of a sufficiently large cavity, where the influence of the lateral boundaries is weak and the periodic approximation remains valid.

It should be emphasised that the comparison with the experimental data reproduced from Bernard *et al.* (2017) is intended to validate the predicted nodal structures on the XY plane only. Since the reported experimental observations are obtained from the top-view imaging of a conventional SSAW configuration, they provide direct information about the in-plane particle distribution patterns and thus enable quantitative comparison of the planar nodal geometries. However, they do not constitute a direct experimental validation of the dual-substrate 3-D configuration considered in the present work. Instead, the out-of-plane nodal structure along the z-direction is examined separately in § 3.3 through comparison between the theoretical prediction and numerical simulation.

3.3. *The PN locations along the z-direction*

As discussed in the previous section, a planar pressure nodal plane perpendicular to the z-axis is defined by $f_2(z) = 0$, written as

$$\frac{W_t \exp\left(i\varphi_z\right) - W_b \exp\left(-iHk_\perp\right)}{\sin\left(Hk_\perp\right)} \cos\left(zk_\perp\right) - iW_b \exp\left(-izk_\perp\right) = 0. \tag{3.6}$$

Let the imaginary and real parts of (3.6) be equal to zero

https://doi.org/10.1017/jfm.2026.11970 Published online by Cambridge University Press

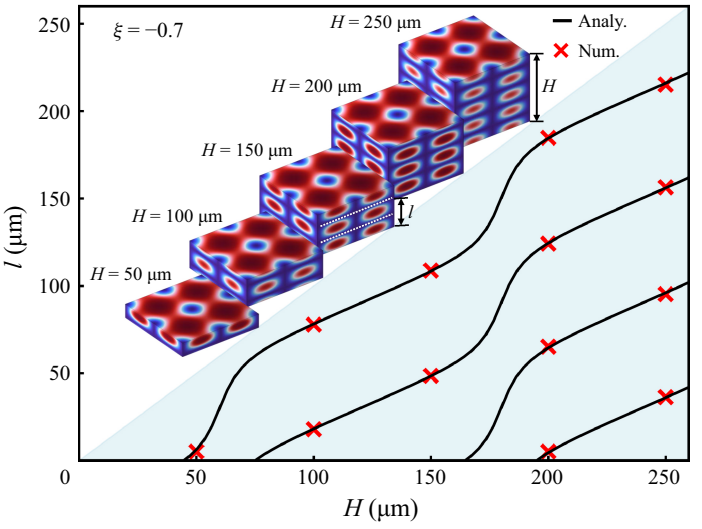


Figure 6. Influence of the fluid cavity height H on the out-of-plane PN position l. The amplitude ratio is set to $\xi = -0.7$. Red crosses denote the nodal positions extracted from simulations, and the black solid curves show the analytical prediction of l as a function of H. The region with light-blue background indicates the physically meaningful fluid domain, and the theoretical solutions fall outside this region are not considered.

$$\begin{cases} 0 = W_t \cos(\varphi_z)\cos(zk_\perp) - W_b \cos((H-z)k_\perp), & (3.7a) \\ 0 = W_t \sin(\varphi_z). & (3.7b) \end{cases}$$

The condition for (3.7*b*) to hold is $\varphi_z = n\pi$, $n \in \mathbb{Z}$. Since $\varphi_z = (2n+1)\pi$ and $\varphi_z = 2n\pi$ simply change the sign of $\cos(\varphi_z)$ in (3.7*a*), both sets of values satisfy the equation. Therefore, we take $\varphi_z = 0$ for simplicity and define a non-dimensional amplitude ratio between SAWs on the top and bottom substrate $\xi = W_t/W_b$, which allows us to rewrite (3.7*a*) as

$$l = z|_{p_1=0} = \frac{1}{k_\perp}\arctan\left(\frac{\xi - \cos(Hk_\perp)}{\sin(Hk_\perp)}\right) + \frac{n\pi}{k_\perp}, \quad n \in \mathbb{Z}, \tag{3.8a}$$

where l is the position where nodal plane intersects z-axis. Inverting (3.8*a*) with respect to the SAW amplitude ratio ξ yields

$$\xi = \frac{W_t}{W_b} = \frac{\cos((H-l)k_\perp)}{\cos(lk_\perp)}. \tag{3.8b}$$

Equation (3.8*a*) enables direct calculation of the vertical nodal-plane position l for acoustofluidic devices with arbitrary channel height H and SAW amplitude ratio ξ. Conversely, if one aims to manipulate the location l of the vertical nodal plane, (3.8*b*) can be applied to determine the corresponding amplitude ratio ξ.

Firstly, the influence of channel height H on the nodal-plane position l is investigated in figure 6. By using a representative amplitude ratio $\xi = -0.7$, black curves in figure 6 illustrate the theoretical nodal-plane position l as a function of channel height H. The numerical simulation results, denoted by red crosses, show a maximum deviation of less than 0.5 μm against the theoretical calculation, demonstrating good agreement. The term $n\pi/k_\perp$ in (3.8*a*) indicates a series of equidistant curves, consistent with numerical observations of multiple PNs spaced by $\pi/k_\perp = 60\,\mu\text{m}$ in channels with $H > 100\,\mu\text{m}$ ($k_\perp = 52395\,\text{m}^{-1}$ is derived from (2.35)). Furthermore, the dependence on $\cos(Hk_\perp)$

https://doi.org/10.1017/jfm.2026.11970 Published online by Cambridge University Press

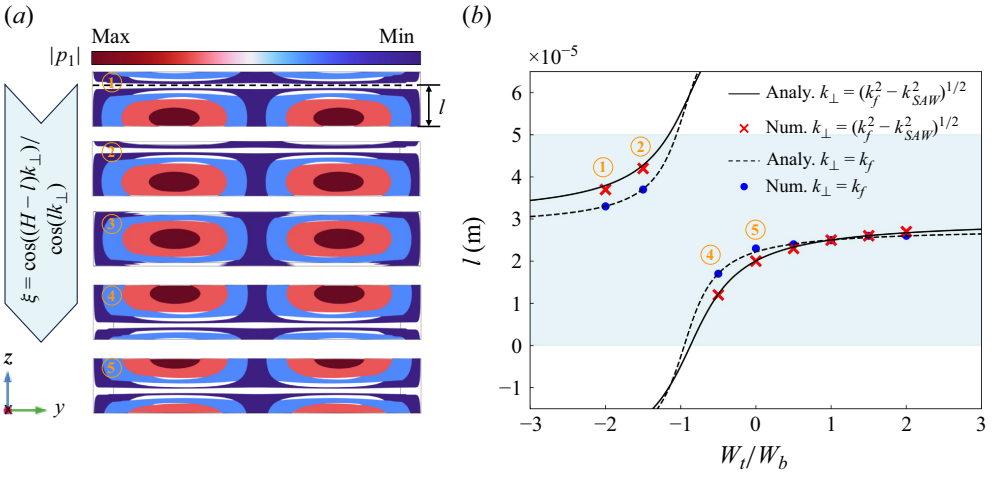


Figure 7. Influence of the amplitude ratio ξ on the out-of-plane PN position l. Panels ①–⑤ in (a) show cross-sectional views of representative simulated acoustic pressure fields under different amplitude ratios ξ. In (b), the solid black curve gives the analytical prediction for a water-filled cavity with sinusoidally vibrating SAWs on substrates, and the red crosses mark the corresponding finite-element simulation results. The dashed black curve shows the idealised limit in which the substrates vibrate rigidly and $k_\perp = k_f$, and the blue circles indicate the numerical results obtained under this limit.

and $\sin(Hk_\perp)$ implies a periodicity of $Hk_\perp = 2\pi$, and therefore, channels with a height difference of $\Delta H = 2\pi/k_\perp = 120\,\mu\text{m}$ will exhibit vertical nodal planes at identical positions. With this theoretical framework, (3.8*a*) offers rigorous design guidelines for acoustofluidic devices that require precise out-of-plane acoustic PN manipulation.

In addition to the geometric effects, the amplitude ratio between SAWs on the upper and lower substrates ξ also plays a critical role in controlling the location of the out-of-plane pressure nodal surface. Figure 7 illustrates the qualitative and quantitative results of the calculated nodal-plane positions l for a range of amplitude ratios ξ. The channel height H is fixed at $50\,\mu\text{m}$ for clarity, as only a single nodal plane is presented at this height. The solid lines represent the theoretically calculated nodal-plane positions, while the red crosses indicate the simulation results. Due to the significant variation in nodal position l when ξ spans from -2 to 1, seven, equally spaced amplitude ratios (with an interval of 0.5) were selected for numerical simulation across this range. The maximum deviation between theory and simulation is less than $0.5\,\mu\text{m}$, demonstrating excellent agreement.

A particular interesting case occurs when $\xi = -1$, corresponding to antiphase vibration of the upper and lower substrates. Under this condition, the central region of the fluid experiences simultaneous compression and extension due to the influences from both the upper and lower substrates, resulting in a higher pressure in the channel mid-plane. This behaviour is consistent with the formation of ANs in the central region and PNs near the bottom and the ceiling of channel, as demonstrated in figure 7(*a*).

In the previous derivations of acoustic field for inviscid fluids, the parameter $k_\perp$ is particularly defined in (2.35) and adopted throughout our work. Its physical significance has been previously discussed in detail by Li *et al.* (2023), and here we briefly clarify its relation to the Rayleigh leakage angle. According to the Huygens–Fresnel principle (Devendran *et al.* 2017), a SAW propagating on a solid substrate experiences refraction when it enters the fluid. The refraction angle, namely Rayleigh angle, is determined by the wavenumber in water $k_f = (\omega/c)$ and the wavenumber on the substrate k_{SAW}. Following

https://doi.org/10.1017/jfm.2026.11970 Published online by Cambridge University Press

the notations in Li *et al.* (2023), the Rayleigh angle is expressed as

$$\theta_R = \arcsin\left(\frac{k_{SAW}}{k_f}\right). \tag{3.9}$$

When a pair of counter-propagating travelling surface acoustic waves interferes on the same substrate, both wavefronts refract as they enter the fluid. The wavefronts of the leaked SAWs in the fluid then interfere to form a standing acoustic field, whose effective wavenumber is

$$k_\perp = \frac{k_{SAW}}{\tan(\theta_R)} = \frac{k_{SAW}}{\tan\left(\arcsin(k_{SAW}/k_f)\right)} = \sqrt{k_f^2 - k_{SAW}^2}. \tag{3.10}$$

The result is equivalent to the definition of $k_\perp$ in (2.35), thereby confirming the consistency between the present formulation and the previous result reported in Li *et al.* (2023).

Equation (3.9) demonstrates that a smaller k_{SAW} results in a smaller Rayleigh angle. Therefore, in the limiting case when $k_{SAW} \to 0$, the SAW propagation along the substrate undergoes negligible refraction when it couples into the fluid. Physically, this corresponds to $\lambda_{SAW} \to \infty$, such that the substrates can be interpreted as rigid 'pistons' oscillating with high frequency along the z-axis (normal to the surface), and the leaked waves behave as a BAW. Figure 7 shows the calculated nodal positions under this limit, demonstrating a high degree of agreement between the theory and simulation.

3.4. *Viscous effects*

While (2.42) and (2.43) can accurately describe acoustofluidic phenomena for most fluids, they may be insufficient for scenarios involving highly viscous fluid or demanding high computational accuracy. For instance, in petroleum processing during oil fractionation (Luo *et al.* 2021; Fasano *et al.* 2025) and biomedical engineering for cell sorting in viscous fluids such as blood plasma (Lim *et al.* 2025), the incorporation of viscosity via (2.31) and (2.32) provides a more precise description of the underlying physics. Specifically, to examine the boundary-layer effect in water, figure 8 presents a direct comparison of the first-order velocity component u_1 under viscous and inviscid conditions. As shown in figure 8(a), the overall standing-wave structure and the order of magnitude of u_1 remain similar in the two cases, indicating that viscosity does not fundamentally alter the overall acoustic field. However, clear differences appear in the immediate vicinity of the vibrating substrates, as highlighted in figures 8(b) and 8(c), where the viscous solution satisfies the no-slip condition and develops a rapid near-wall transition that is absent in the inviscid solution. The penetration depth (Marques & Tomaz Da Silva 2025) δ can be estimated to be

$$\delta = \sqrt{2\mu/\rho_0\omega}. \tag{3.11}$$

For liquid water, $\delta = 0.16\,\mu\text{m}$, which indicates that the boundary-layer effects are confined within a very thin region adjacent to the substrate. As detailed by Doinikov *et al.* (2017), the pronounced velocity overshoot near the edge of the boundary layer arises from the transition between the thin viscous layer and the bulk region, which is evident in figures 8(b) and 8(c). Therefore, the viscosity of water does not change the global standing-wave pattern, but it modifies the near-wall velocity distribution and thereby influences the nodal positions in the z-direction.

This behaviour can also be interpreted from the eigenvalue analysis in (2.23). As discussed in § 2.5, the eigenvalue $\lambda_4 = (6428 + 6428i)\,\text{mm}^{-1}$ is associated with the

https://doi.org/10.1017/jfm.2026.11970 Published online by Cambridge University Press

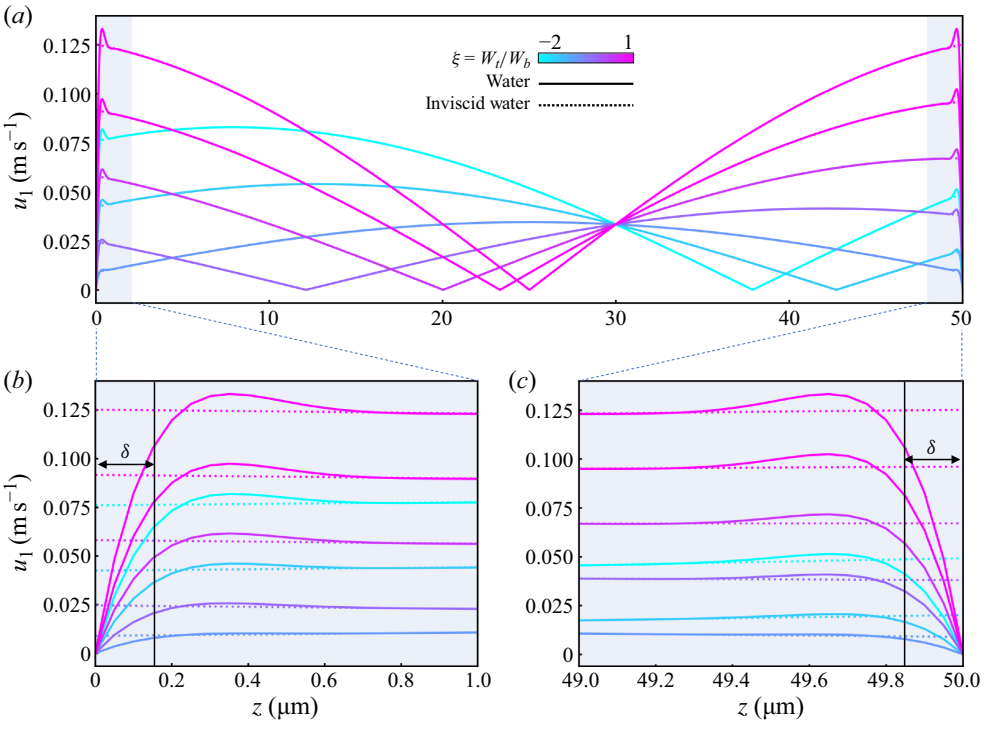


Figure 8. Boundary-layer velocity profiles for water under viscous and inviscid conditions. Solid lines denote the viscous solution, and dotted lines denote the inviscid solution. (*a*) First-order velocity component u_1 along the z-axis for different amplitude ratios ξ. (*b*) Magnified view near the bottom substrate. (*c*) Magnified view near the top substrate.

viscous effect and contains a large real component, indicating rapid spatial attenuation. In contrast, $\lambda_1 = (0.004 + 52.4i)\,\mathrm{mm}^{-1}$, which describes the inviscid effect, has a negligible real component. Owing to the large real component of λ_4, viscous effects decay exponentially to almost zero in water, whereas the waves in the inviscid bulk region represented by λ_1 can propagate over considerable distances without significant attenuation. This explains why the viscous and inviscid solutions remain close in the bulk region while exhibiting substantial differences near the fluid–substrate interfaces.

For most liquids commonly encountered in acoustofluidic applications, the influence of viscosity can be quantified by the viscous penetration depth δ and the associated acoustic attenuation. Under typical MHz-frequency conditions, δ remains much smaller than the channel height and the acoustic wavelength for low-to-moderately viscous fluids. In this situation, viscous effects are mainly confined to the thin boundary layers adjacent to the vibrating substrates, while the acoustic field in the central part of the cavity remains virtually inviscid. As viscosity increases further, however, the penetration depth grows and viscous attenuation becomes more pronounced, so that the effect of viscosity will no longer be restricted to the immediate vicinity of the boundaries but modifies the flow over the whole domain. To illustrate this transition from the boundary-layer-confined viscous effects to more substantial cavity-scale influence, we next consider engine oil as a representative highly viscous fluid.

https://doi.org/10.1017/jfm.2026.11970 Published online by Cambridge University Press

To further investigate how strong viscosity influences the nodal-plane positions in the acoustic field, we considered a highly viscous material, namely engine oil. The material properties of the engine oil employed in this study were $\rho_0 = 887.59\ \mathrm{kg\ m^{-3}}$, $c = 1000\ \mathrm{m\ s^{-1}}$ (Rooke *et al.* 2023), $\mu = 0.79017\ \mathrm{Pa\ s}$ (Alhouli *et al.* 2015; Tripathi & Vinu 2015; Barcenas & Miller 2025) and $\mu_B = 0.79\ \mathrm{Pa \cdot s}$. Since precise measurements of μ_B are unavailable, it was approximated by referring to μ. To assess the sensitivity of the results to this approximation, additional calculations were performed with $\mu_B = 0.4$ and $1.2\ \mathrm{Pa \cdot s}$, i.e. $\pm 50\,\%$ around the adopted value. The resulting changes in λ_1 and λ_2 were less than $1\,\%$ in magnitude and less than 1° in inclination angle, while the changes in λ_3 and λ_4 were below 10^{-4} in magnitude, with negligible angular variation. These results indicate that the conclusions of the present analysis are insensitive to the assumed bulk viscosity.

The decomposition in (3.1) can also be applied to (2.32), yielding

$$\begin{cases} 0 = f_{1,\mathrm{vis}}\,(x,\,y) \cdot f_{2,\mathrm{vis}}(z), \\ f_{1,\mathrm{vis}}\,(x,\,y) = \cos\,(k_{SAW}x - \varphi_x) + \exp\,(-i\varphi_\Delta)\cos\left(k_{SAW}y - \varphi_y\right), \\ f_{2,\mathrm{vis}}(z) = \sum_{j=1,2,3,4} \left(\dfrac{i\omega\rho_0 + \mu k_{SAW}^2 - \mu\lambda_j^2}{\lambda_j(R-\mu)} \right) \\ \qquad \left(C_{b,j}W_b + C_{t,j}W_t \exp\,(i\varphi_z)\right) \exp\left(\lambda_j z\right). \end{cases} \tag{3.12}$$

Equation (3.12) shows that, for highly viscous fluids, the full 3-D pressure nodal surface can be decomposed into two independent nodal surface systems. From (3.1) and (3.12), $f_{1,\mathrm{vis}}(x,\,y) = f_1(x,\,y)$, indicating that the shape of nodal surface parallel to the z-axis is identical for inviscid and viscous conditions. However, the presence of real components in the eigenvalues λ_1 and λ_2 under highly viscous cases (as shown in the table in figure 3) directly cause the nodal system $f_{2,\mathrm{vis}}(z)$ values to deviate from those in inviscid fluid (described by $f_2(z)$ in (3.1)). Therefore, the introduction of viscosity mainly affects the PN locations along the z-direction. In figure 9, the acoustic pressure amplitude along the z-direction is captured under different cases. The black solid lines indicate the inviscid condition obtained by (2.43), while the blue and red dashed lines denote the viscous scenarios calculated from (2.32) with and without a phase correction, respectively. From figure 9, substantial discrepancies near the nodal positions can be observed between the inviscid and viscous curves. This indicates that the inviscid formulation in (2.43) is no longer sufficient to accurately capture the acoustic field under highly viscous conditions.

As depicted in figure 9, the blue dashed lines highlight another challenge posed by high-viscosity fluids: the absence of locations where the acoustic pressure reaches an exact zero. In an inviscid fluid, the two counter-propagating waves along the out-of-plane direction do not undergo amplitude attenuation, and their superposition always produces exact zero-pressure locations regardless of the amplitude ratio ξ, which can also be concluded from (3.8). For viscous fluid, however, solely tunning amplitude ratio ξ cannot guarantee a zero pressure at the nodes, thereby impacting the efficiency and accuracy of acoustofluidic manipulation. To restore a zero pressure on the nodal plane in viscous environment, one can adjust φ_z corresponding to the amplitude ratio ξ. Specifically, setting $f_{2,\mathrm{vis}}(z)$ in (3.12) to zero yields

https://doi.org/10.1017/jfm.2026.11970 Published online by Cambridge University Press

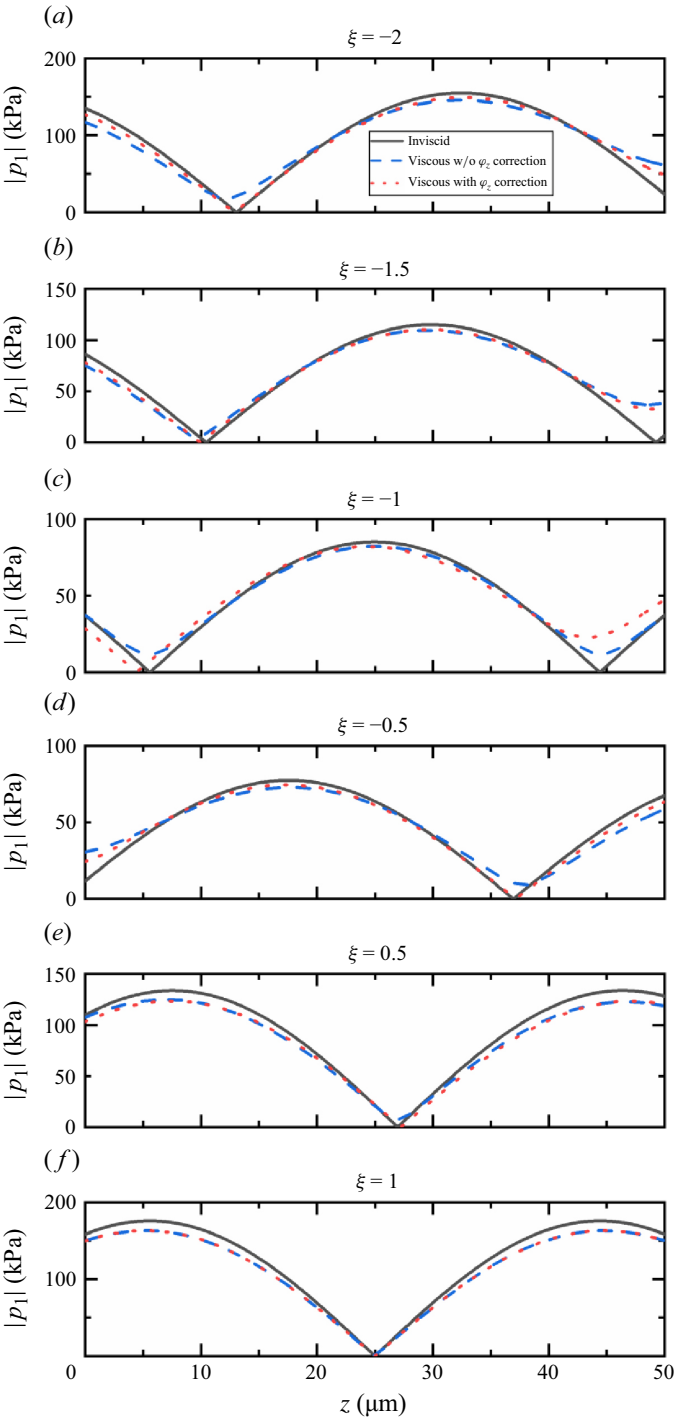


Figure 9. Acoustic pressure profiles along the z-direction for a high-viscosity fluid under different amplitude ratios ξ. The black solid curves are the inviscid prediction from (2.43), the blue dashed curves show the viscous results from (2.32) and the red dotted curves are viscous prediction obtained from (2.32) with additional phase compensation φ_z to reduce the viscosity-induced residual pressure at the nodal positions.

https://doi.org/10.1017/jfm.2026.11970 Published online by Cambridge University Press

$$\exp(i\varphi_z) = -\frac{1}{\xi}\frac{\sum_{j=1,2,3,4}\left(\dfrac{i\omega\rho_0 + \mu k_{SAW}^2 - \mu\lambda_j^2}{\lambda_j(R-\mu)}\right) C_{b,j}\exp(\lambda_j l)}{\sum_{j=1,2,3,4}\left(\dfrac{i\omega\rho_0 + \mu k_{SAW}^2 - \mu\lambda_j^2}{\lambda_j(R-\mu)}\right) C_{t,j}\exp(\lambda_j l)}, \tag{3.13a}$$

$$1 = \frac{1}{|\xi|}\left|\left|\frac{\sum_{j=1,2,3,4}\left(\dfrac{i\omega\rho_0 + \mu k_{SAW}^2 - \mu\lambda_j^2}{\lambda_j(R-\mu)}\right) C_{b,j}\exp(\lambda_j l)}{\sum_{j=1,2,3,4}\left(\dfrac{i\omega\rho_0 + \mu k_{SAW}^2 - \mu\lambda_j^2}{\lambda_j(R-\mu)}\right) C_{t,j}\exp(\lambda_j l)}\right|\right|. \tag{3.13b}$$

Equation (3.13*b*) determines whether a zero-pressure nodal plane can exist and where plane is located, while (3.13*a*) gives the required phase compensation φ_z to achieve a zero pressure at the nodal plane. Since (3.13*b*) is a function of only l, the Newton–Raphson method is implemented to determine the nodal-plane position l. Then, the nodal-plane position l acquired from (3.13*b*) is substituted into (3.13*a*) to obtain the corresponding compensation phase, φ_z.

By adjusting the compensation phase φ_z, as illustrated by the red dashed line in figure 9, the sharp zero-pressure wells can be restored. This confirms that amplitude–phase modulation is essential for achieving zero acoustic pressure nodal planes in highly viscous fluids. Furthermore, it is worth noting that adjusting φ_z does not provides a global correction, instead it only minimises acoustic pressure at a specific targeted PN. For example, when $\xi = -1$, two PNs appear at $z = 6$ and $z = 44\,\mu$m. Appling compensation to the PN at $z = 6\,\mu$m inevitably increases the pressure at $z = 44\,\mu$m. This selective compensation strategy for specific nodal positions suggests a potential approach for targeted acoustofluidic particle manipulation in viscous environments.

3.5. *Second-order velocity field*

The analytical formulation developed in § 2.7 is further validated by comparing the predicted second-order acoustic streaming field with numerical simulations. The same fluid domain and material parameters as those used in the first-order validation are adopted. The first-order acoustic fields for the viscous fluid obtained from (2.31) and (2.32) are used to construct the nonlinear forcing terms in (2.44), and the resulting acoustic streaming field is calculated analytically from the solution given in (2.65). A representative two-dimensional (x, z) subproblem is considered to validate the second-order streaming formulation by comparing the analytical results with the numerical simulations. Figure 10 shows the second-order velocity component w_2 together with the corresponding streamlines for two representative amplitude ratios, $\xi = 1$ and $\xi = -0.7$.

As shown in figure 10(*a*), when $\xi = 1$, the streaming field forms a periodic array of counter-rotating vortices. The magnitude of w_2 reaches approximately $42\,\mu\text{m s}^{-1}$, which is several orders of magnitude smaller than the first-order acoustic velocity, consistent with its second-order origin. The analytical profiles along the selected cutlines agree well with the numerical results, with ($R^2 = 0.98$) for both comparisons. For $\xi = -0.7$, as shown in figure 10(*b*), the streaming pattern is modified by the change in the relative vibration amplitude of the two substrates. The maximum magnitude of w_2 decreases to approximately $12\,\mu\text{m s}^{-1}$, and the vortex structure becomes less symmetric compared with the case of $\xi = 1$. Nevertheless, the analytical solution still captures the numerical streaming profiles accurately, with $R^2 = 0.997$ and $R^2 = 0.98$ along the two selected cutlines.

https://doi.org/10.1017/jfm.2026.11970 Published online by Cambridge University Press

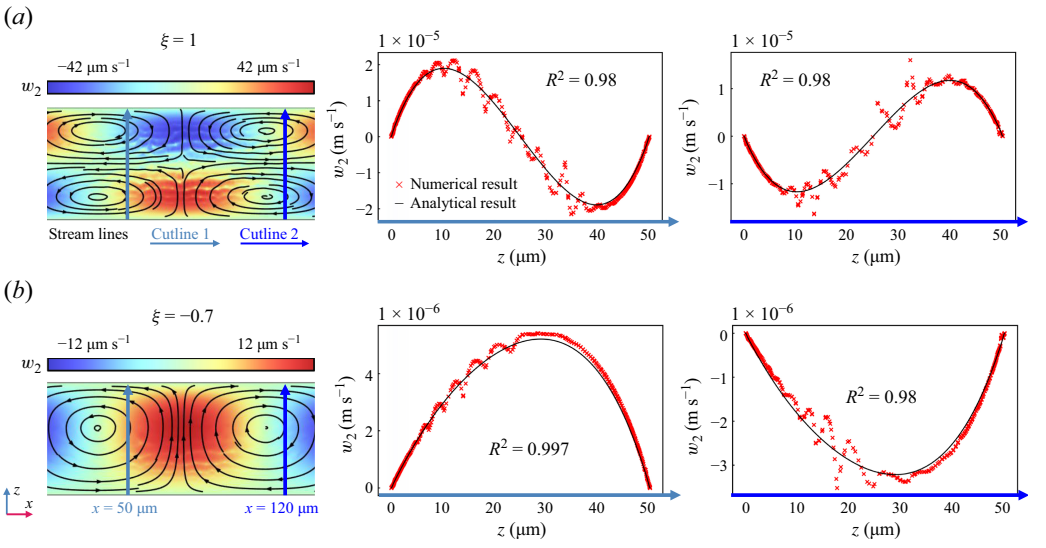


Figure 10. Validation of the analytical solution for the second-order acoustic streaming field. Contours show the second-order velocity component (w_2), with streamlines indicating the corresponding quasi-steady streaming patterns. Red crosses denote the numerical results, and black solid lines denote the analytical solutions along the selected cutlines. (*a*) Results for $\xi = 1$. (*b*) Results for $\xi = -0.7$.

These comparisons demonstrate that the frequency-domain perturbation method can accurately predict not only the first-order acoustic field but also the induced time-averaged second-order streaming flow. It should be noted that acoustic streaming is highly sensitive to the near-wall boundary-layer flow. Therefore, in the numerical simulations, the mesh was refined near the solid boundaries to better resolve the boundary-layer contribution to the streaming field, while a relatively coarser mesh was used in the central region of the channel to reduce the computational cost. This mesh distribution is also reflected in figure 10. Near the boundaries, the numerical results vary smoothly and agree closely with the analytical predictions. In contrast, in the central region, where the mesh is relatively sparse, the numerical profiles exhibit larger local fluctuations and deviations from the analytical curves. These discrepancies are therefore likely associated with the finite numerical resolution in the central region, while the overall agreement shown in figure 10 confirms the reliability of the proposed analytical framework for describing the representative 2-D acoustic streaming subproblem induced by SAW excitation.

4. Conclusions

This paper presented a theoretical analysis of the 3-D acoustofluidic fields actuated by dual-sided SSAWs at the two boundaries perpendicular to the z-axis. A frequency-domain perturbation framework was developed to obtain both the first-order acoustic field and the time-averaged second-order acoustic streaming field. The derived theoretical solutions agree well with the numerical simulations, yielding a coefficient of determination (R^2) greater than 0.99 for the first-order acoustic field and no less than 0.98 for the second-order streaming profiles. Detailed analyses of the derived equations provided valuable insights into the pressure-field characteristics within the microfluidic cavity, which are consistent with the experimental observations reported in Bernard *et al.* (2017) and shed light on the controlled movements of microparticles suspended within the fluid cavity. We analytically

https://doi.org/10.1017/jfm.2026.11970 Published online by Cambridge University Press

determined the pressure nodal positions and accounted for the effects of cavity geometry and the amplitude ratio of the two actuation SSAWs. For inviscid fluids, we found that the nodal plane along the z-axis can be controlled solely by modifying the amplitude of the SSAWs. Furthermore, we studied the viscous effects in our theoretical framework and investigated the velocity profile and the thickness of the viscous boundary layers. The viscous effects were found to remain localised, while the bulk fluid remains largely inviscid. In addition to the first-order viscous solution, the representative 2-D second-order acoustic streaming subproblem was also formulated and validated, demonstrating that the proposed perturbation method can predict the induced quasi-steady streaming vortices and their dependence on the relative actuation amplitude. In order to achieve the precise out-of-plane manipulation of the pressure nodal positions and the exact zero-pressure conditions at the nodes in viscous flows, the combined tuning of the amplitude and phase of the actuation SSAWs is required. This approach is crucial for maximising the efficiency of microparticle manipulation. Our findings gain a solid understanding of the complex response of the flow field to the acoustic actuation at the boundary and build a theoretical foundation for pressure-node regulation, acoustic streaming prediction and 3-D acoustofluidic control of microparticles.

Supplementary material. Supplementary material is available at https://doi.org/10.1017/jfm.2026.11970.

Acknowledgements. We are grateful to the support by the Intergovernmental Key Program for the National Key Research and Development Program of China (2024YFE0115200) and the Royal Society International Exchanges Scheme (IEC\NSFC\242411).

Declaration of interests. The authors have no conflict to disclose.

Data availability statement. The data that support the findings of this study are available from the corresponding author upon reasonable request.

Author contributions. Y.L. and Z.L. conceived the original idea and designed the study. D.L. and Z.L. developed the theoretical formulation and carried out the analytical derivations. Y.Z. and J.Z. performed the numerical simulations and validation. C.F. contributed to and interpretation of the acoustofluidic results. X.Y. and D.L. supervised the project and provided guidance on the theoretical analysis and physical interpretation. All authors contributed to discussing the results, revising the manuscript and approving the final version.

References

ALHOULI, Y., ALSHAMMRI, A.G., ABED, A.I. & ALALI, S.A. 2015. Mathematical modeling of engine new and used oils. *Intl J. Res. Adv. Engng Technol.* **1** (1), 18–22.

BARCENAS, L. & MILLER, R.E. 2025 An integrated computational fluid dynamics and chemical kinetics modeling for predicting oil degradation in maritime diesel engines. *Adv. Mech. Engng* **17** (12), 1–22.

BAUDOIN, M. & THOMAS, J.-L. 2020 Acoustic tweezers for particle and fluid Micromanipulation. *Annu. Rev. Fluid Mech.* **52**, 205–234.

BERNARD, I., DOINIKOV, A.A., MARMOTTANT, P., RABAUD, D., POULAIN, C. & THIBAULT, P. 2017 Controlled rotation and translation of spherical particles or living cells by surface acoustic waves. *Lab on a Chip* **17**, 2470–2480.

DEVENDRAN, C., COLLINS, D.J., AI, Y. & NEILD, A. 2017 Huygens-fresnel acoustic interference and the development of robust time-averaged patterns from traveling surface acoustic waves. *Phys. Rev. Lett.* **118**, 154501.

DING, X., LIN, S.-C.S., KIRALY, B., YUE, H., LI, S., CHIANG, I.-K., SHI, J., BENKOVIC, S.J. & HUANG, T.J. 2012 On-chip manipulation of single microparticles, cells, and organisms using surface acoustic waves. *Proc. Natl Acad. Sci. USA* **109**, 11105–11109.

DOINIKOV, A.A. 1994 Acoustic radiation pressure on a compressible sphere in a viscous fluid. *J. Fluid Mech.* **267**, 1–22.

https://doi.org/10.1017/jfm.2026.11970 Published online by Cambridge University Press

DOINIKOV, A.A., THIBAULT, P. & MARMOTTANT, P. 2017 Acoustic streaming in a microfluidic channel with a reflector: case of a standing wave generated by two counterpropagating leaky surface waves. *Phys. Rev. E* **96**, 013101.

ECKART, C. 1948 Vortices and streams caused by sound waves. *Phys. Rev.* **73**, 68–76.

FASANO, M., LI, Y., DIEZ, J.A., D'ADDESA, J., MANOR, O., CUMMINGS, L. & KONDIC, L. 2025 Modelling the dynamics of an oil drop driven by a surface acoustic wave in the underlying substrate. *J. Fluid Mech.* **1022**, A49.

FRIEND, J. & YEO, L.Y. 2011 Microscale acoustofluidics: microfluidics driven via acoustics and ultrasonics. *Rev. Mod. Phys.* **83**, 647–704.

HSU, J.-C. & LIAO, K.-L. 2025 Driving rotational circulation in a microfluidic chamber using dual focused surface-acoustic-wave beams. *Micromachines* **16**, 140.

JANNESAR, E.A. & HAMZEHPOUR, H. 2021 Acoustic tweezing of microparticles in microchannels with sinusoidal cross sections. *Sci. Rep.* **11**, 17902.

JO, M.C. & GULDIKEN, R. 2012 Active density-based separation using standing surface acoustic waves. *Sens. Actuators Phys.* **187**, 22–28.

KING, L.V. 1934 On the acoustic radiation pressure on spheres. *Proc. R. Soc. Lond. Math. Phys. Sci.* **147**, 212–240.

KÖSTER, D. 2007 Numerical simulation of acoustic streaming on surface acoustic wave-driven biochips. *SIAM J. Sci. Comput.* **29**, 2352–2380.

LI, J., CRIVOI, A., PENG, X., SHEN, L., PU, Y., FAN, Z. & CUMMER, S.A. 2021 Three dimensional acoustic tweezers with vortex streaming. *Commun. Phys.* **4**, 113.

LI, Y., LI, Z., LIANG, D., GAO, B. & FU, C. 2026 Acoustic streaming enhanced micromixing in microfluidic channels. *J. Hydrodyn.* **38**, 87–94.

LI, Y., LI, Z., WEI, Z., WANG, Y., NIU, X. & LIANG, D. 2025*a* Efficient particle aggregation through SSAW phase modulation. *Micromachines* **16**, 910.

LI, Y., LIANG, D., KABLA, A., ZHANG, Y., MA, J. & YANG, X. 2025*b* Dependence of acoustophoretic aggregation on the impedance of microchannel's walls. *Comput. Meth. Programs Biomed.* **260**, 108530.

LI, Y., LIANG, D., KABLA, A., ZHANG, Y. & YANG, X. 2023 Sensitivity of acoustofluidic particle manipulation to microchannel height in standing surface acoustic wave-based microfluidic devices. *Phys. Fluids* **35**, 122018.

LIGHTHILL, S.J. 1978 Acoustic streaming. *J. Sound Vib.* **61**, 391–418.

LIM, H., HONG, S., CHO, S., HAN, B., KIM, J.Y., KIM, J. & NAM, J. 2025 Advanced design of indented-standing surface acoustic wave (i-SSAW) device for platelet-derived microparticle separation from whole blood. *Sens. Actuators B Chem.* **423**, 136742.

LUO, X., GONG, H., HE, Z., ZHANG, P. & HE, L. 2021 Recent advances in applications of power ultrasound for petroleum industry. *Ultrason. Sonochem.* **70**, 105337.

MARQUES, A.D.S. & TOMAZ DA SILVA, G. 2025 Vortex modes in acoustofluidic cylindrical resonators. *J. Fluid Mech.* **1015**, A34.

MELDE, K., MARK, A.G., QIU, T. & FISCHER, P. 2016 Holograms for acoustics. *Nature* **537**, 518–522.

MULLER, P.B., ROSSI, M., MARIN, A.G., BARNKOB, R., AUGUSTSSON, P., LAURELL, T., KAEHLER, C.J. & BRUUS, H. 2013 Ultrasound-induced acoustophoretic motion of microparticles in three dimensions. *Phys. Rev. E.* **88**, 023006.

NAM, J. & LIM, C.S. 2018 Micromixing using swirling induced by three-dimensional dual surface acoustic waves (3D-dSAW). *Sens. Actuators B Chem.* **255**, 3434–3440.

NAMA, N., BARNKOB, R., MAO, Z., KÄHLER, C.J., COSTANZO, F. & HUANG, T.J. 2015 Numerical study of acoustophoretic motion of particles in a PDMS microchannel driven by surface acoustic waves. *Lab on a Chip* **15**, 2700–2709.

RAYLEIGH, L. 1884 On the circulation of air observed in Kundt's tubes, and on some allied acoustical problems. *Phil. Trans. R. Soc. Lond.* **175**, 1–21.

ROOKE, J., BRUNSKILL, H., LI, X., TAGHIZADEH, S., HUNTER, A., HE, S., LU, X. & DWYER-JOYCE, R.S. 2023 Piston ring oil film thickness measurements in a four-stroke diesel engine during steady-state, start-up and shut-down. *Intl J. Engng Res.* **24**, 1499–1514.

SHEN, L., *et al.* 2024 Joint subarray acoustic tweezers enable controllable cell translation, rotation, and deformation. *Nat. Commun.* **15**, 9059.

STRINGER, M., *et al.* 2023 Methodologies, technologies, and strategies for acoustic streaming-based acoustofluidics. *Appl. Phys. Rev.* **10**, 011315.

SUN, C., *et al.* 2020 Gallium nitride: a versatile compound semiconductor as novel piezoelectric film for acoustic tweezer in manipulation of cancer cells. *IEEE Trans. Electron Devices* **67**, 3355–3361.

https://doi.org/10.1017/jfm.2026.11970 Published online by Cambridge University Press

SUN, X., TAN, W. & MAN, Y. 2025 Trapping microswimmers in acoustic streaming flow. *J. Fluid Mech.* **1008**, A32.

TRIPATHI, A. & VINU, R. 2015 Characterization of thermal stability of synthetic and semi-synthetic engine oils. *Lubricants* **3**, 54–79.

WANG, H., *et al.* 2023 Modelling hybrid acoustofluidic devices for enhancing nano- and micro-particle manipulation in microfluidics. *Appl. Acoust.* **205**, 109258.

WESTERVELT, P.J. 1953 The theory of steady rotational flow generated by a sound field. *J. Acoust. Soc. Am.* **25**, 60–67.

https://doi.org/10.1017/jfm.2026.11970 Published online by Cambridge University Press